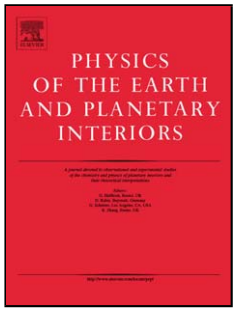

Title: Structure of the crust beneath the Southeastern Tibetan Plateau from Teleseismic Receiver Functions

Authors: Lili Xu, Stéphane Rondenay, Robert D. van der Hilst

PII: S0031-9201(07)00202-6
DOI: doi:10.1016/j.pepi.2007.09.002
Reference: PEPI 4868

To appear in: *Physics of the Earth and Planetary Interiors*

Received date: 23-8-2006
Revised date: 10-9-2007
Accepted date: 11-9-2007

Please cite this article as: Xu, L., Rondenay, S., van der Hilst, R.D., Structure of the crust beneath the Southeastern Tibetan Plateau from Teleseismic Receiver Functions, *Physics of the Earth and Planetary Interiors* (2007), doi:10.1016/j.pepi.2007.09.002

Structure of the crust beneath the Southeastern Tibetan Plateau from Teleseismic Receiver Functions

Lili Xu*, Stéphane Rondenay, Robert D. van der Hilst

Department of Earth, Atmospheric, and Planetary Sciences, Massachusetts Institute of Technology, 77 Massachusetts Avenue, Cambridge, MA, USA 02139

*Corresponding author: lilixu@mit.edu, Telephone: 617-252-1974, Fax: 617-258-0620

Abstract

Southeastern Tibet marks the site of presumed clockwise rotation of the crust due to the India-Eurasian collision and abutment against the stable Sichuan basin and South China block. Knowing the structure of the crust is a key to better understanding crustal deformation and seismicity in this region. Here, we analyze recordings of teleseismic earthquakes from 25 temporary broadband seismic stations and one permanent station using the receiver function method. We find that crustal thickness decreases gradually from the Tibetan plateau proper to the Sichuan basin and Yangtze platform but that significant (intra-)crustal heterogeneity exists on shorter lateral scales (<1000 km). Most receiver functions reveal a time shift of ~0.2s in the direct *P* arrival and negative phases between 0 and 5 s after the first arrival. Inversion of the receiver functions yields *S*-velocity profiles marked by near-surface and intra-crustal low-velocity zones (IC-LVZs). The shallow low-velocity zones are consistent with the wide distribution of thick surface sedimentary layers. The IC-LVZ varies laterally in depth and strength; it becomes thinner toward the east and southeast and is absent in the Sichuan basin and the southern part of the Yangtze platform. Results from slant-stacking analysis show a

concomitant decrease in crust thickness from ~60 km in the Songpan-Ganze fold system to ~46 km in the Sichuan basin and ~40 km in the Yangtze platform. High Poisson's ratios (> 0.30) are detected beneath the southeastern margin of Tibet but in the Sichuan basin and southestern Yangtze platform the values are close to the global average. Combined with high regional heat flow and independent evidence for mid-crustal layers of high (electric) conductivity, the large intra-crustal *S*-wave velocity reduction (12–19%) and the intermediate-to-high average crustal Poisson's ratios are consistent with partial melt in the crust beneath parts of southeastern Tibet. These results could be used in support of deformation models involving intra-crustal flow, with the caveat that significant lateral variation in location and strength of this flow may occur.

Keywords: southeastern Tibet, receiver function, Moho discontinuity, *S*-wave velocity profile, Low-velocity zone, partial melt

1. Introduction

Geological structures suggest that deformation in the central part of the Tibetan plateau, directly north of the Indian subcontinent, has largely been the result of north-south convergence (Molnar and Tapponnier, 1975; Rowley, 1996). However, east of the Himalayan syntaxis, the east-west trending structural features of central Tibet bend southeastward as a consequence of the extrusion of crustal elements from central Tibet, their abutment against the Sichuan basin and South China block, and the stress field caused by subduction under the Burma ranges (King et al., 1997; Chen et al., 2000; Wang et al., 2001; Lev et al., 2006). The left-lateral Xianshuihe-Xiaojiang fault system forms the eastern boundary of the clockwise rotation (Avouac and Tapponnier, 1993; Wang and Burchfiel, 2000).

Following Chen et al. (1987) and Wang et al. (2003) we recognize four major geological units southeast of the Tibetan plateau proper: the Yangtze Platform, the Songpan-Ganze fold system, the Sanjiang fold system, and the Bomi-Tengchong fold system (Figure 1). The Songpan-Ganze and Sanjiang fold belts are separated from the Yangtze Platform by the Longmen Shan fault and the Red River fault, respectively. The Sichuan basin is located to the east of the Longmen Shan fault and is part of the Yangtze platform. Surface sediments of up to 10 km thickness are widespread throughout the study region (Leloup et al., 1995; Song and Lou, 1995; Burchfiel and Wang, 2003). The Tengchong area belongs to the Bomi-Tengchong fold system, with volcanic activity in the Cenozoic.

The crustal structure in Tibet has been debated. For example, previous shear-wave splitting studies (e.g., McNamara et al., 1994; Sandvol et al., 1997) indicated that the mantle anisotropy is aligned with surface structures. These results were interpreted by Silver (1996) and Sandvol et al. (1997) to represent, at least in central Tibet, a high degree of mechanical coupling between the upper crust and the upper mantle, or, at least, that the lower crust is strong enough to transfer shear stresses between the crust and mantle over horizontal length scales of tens of kilometers. In contrast, geologic and GPS studies (Burchfiel et al., 1995; Chen et al., 2000; Wang et al., 2001) showed little to no convergence across a large part of eastern Tibet, implying that eastern Tibet has been uplifted without appreciable shortening of the upper crust, and that crustal thickening involved primarily shortening within the deep crust. Royden and co-workers explained this observation as well as the evolution in shape of river streams with a channel flow model in which the deep crust is weak and in which there is little correlation between the

crustal and upper mantle deformation (Royden et al., 1997; Clark and Royden, 2000; Roy and Royden, 2000a and b; Clark et al., 2005).

Regional shear-wave splitting measurements are consistent with some level of decoupling of crust and upper mantle beneath parts of the study region (Lev et al., 2006). The interpretation of teleseismic shear-wave splitting measurements is often ambiguous, however. Indeed, opposite conclusions have been reached from joint modeling of shear-wave splitting and GPS results, using a thin viscous sheet approach (Silver, 1996; Holt, 2000; Flesch et al., 2005).

Receiver function studies in central Tibet (Kind et al., 1996; Nelson et al., 1996; Yuan et al., 1997; Ozacar and Zandt, 2004) presented evidence for a crustal low-velocity zone. This could be, and has been, used in support of the crust-mantle decoupling and middle/lower crustal flow, but to date the observations have been too sparse to determine whether this crustal low-velocity zone extends into the southeastern part of the Tibetan plateau. Moreover, as we will show here, it is likely that neither end-member model is correct and that significant lateral variation exists in the nature of crust-mantle coupling and – if present at all – in the depths where intra-crustal flow might occur.

To date, most estimates of crustal thickness for southeastern Tibet are derived from deep seismic sounding profiles and from the coherence between gravity anomalies and topography (e.g., Lin et al., 1993; Li and Mooney, 1998; Wang et al., 2003). Previous receiver function studies in the Yunnan province (Hu et al., 2003; He et al., 2004) suggest that a crustal low-velocity zone exists in the upper and/or lower crust of the western Yangtze platform. Furthermore, the high average crustal Poisson's ratio of > 0.30 (Hu et al., 2003) for this area suggests the existence of partial melt in the crust (Owens and

Zandt, 1997). Body-wave tomography (Huang et al., 2002; Wang et al., 2003) revealed low-velocity anomalies in the crust and upper mantle of various areas (e.g., the western Sichuan plateau and the Panxi tectonic zone). Such intra-crustal low-velocity zones (IC-LVZs) are also apparent in results of high-resolution surface wave array tomography (Yao et al., 2006, 2007). In combination, these previous studies suggest that the crust beneath southeastern Tibet is highly heterogeneous.

In order to improve the characterization of this heterogeneity we analyze data from a regional network of 25 temporary broadband seismometers (Figure 1). We use receiver function analysis, which has been used previously to characterize the crust (including IC-LVZs) in a variety of tectonic environments (e.g., Langston, 1979; Gurrola et al., 1995; Owens and Zandt, 1997; Yuan et al., 1997; Bostock, 1998; Zorin et al., 2002). We first use a simultaneous deconvolution approach to obtain the average crustal impulse response (Gurrola et al., 1995; Bostock, 1998). Then we use a slant-stacking method to constrain simultaneously the crustal thickness (H) and *P*-to-*S* wave velocity ratio (V_P/V_S) (Zhu and Kanamori, 2000; Chevrot and van der Hilst, 2000). Finally, we derive *S*-wave velocity profiles through least-squares inversion of the receiver function waveforms and simplify the derived models into fewer layered models (Owens et al., 1984; Ammon et al., 1990; Kind et al., 1995). Such inversions have been used in previous studies to image low-velocity layers within the crust (e.g., Kind et al., 1996; Frederiksen et al., 2003; Hetland et al., 2004) and can be used to estimate both the depth to and thicknesses of the IC-LVZs.

2. Methodology

2.1 Receiver functions

The receiver function technique derives a source-equalized teleseismic waveform, in which source, far field path, and instrument effects are removed by deconvolving the vertical component from the radial/transverse components (Langston, 1979; Gurrola et al., 1995; Bostock, 1998). The resulting receiver function waveform is an estimate of the ground's impulse response. For stations MC01-MC25, the gains were the same on all channels, whereas for station KMI they differed by < 3% between channels. No equalization before rotation was performed for the latter due to the small difference in gain, which we believe does not strongly affect our results. In this study, the following processing steps are applied to derive the receiver functions: rotation, deconvolution, moveout correction, stacking, and filtering. First, all teleseismic traces are rotated from an E-N-Z coordinate system to an R-T-Z system (Figure 2). Second, we deconvolve the vertical components from both the radial and transverse components to remove the effects of the source and the instrument. During this process, which is conducted in the frequency domain, we apply a water level to stabilize the spectral division (e.g., Langston, 1979; Bostock, 1998). The water level is adjusted to the quality of the original seismogram and the stability of the equalization; it varies from 10^{-3} to10^{-1}. Third, a Gaussian filter with width of 2.0 Hz is applied in the frequency domain after decovolution to remove high frequency noise in the seismogram. To improve the overall signal-to-noise ratio and ensure stability of the deconvolution process, we simultaneously deconvolve all seismograms along moveout curves, which depend on the horizontal slowness and the depth of phase conversion (Bostock, 1998); this provides an average ground impulse response of the sampling area.

The lateral offset between the surface recording point and conversion point at depth is a function of the ray parameter, the crustal thickness, and the average crustal velocity. For example, for a ray parameter of 0.0586 s/km (*P*-wave from a source at 67° distance), crust thickness of 40 km, and crust velocities V_P = 6.2 km/s and V_S = 3.6 km/s, the P_ms phases sample the Moho ~9 km from the stations, while multiples sample it ~40 km away.

2.2 Slant-stacking method

Crust thickness *H* and average V_P/V_S of the crust can be estimated from the relative timing of *P*-to-*S* conversions and reverberations (see Figure 2). Here, we follow the approach of Zhu and Kanamori (2000) and use the travel times of three phases relative to the direct *P* (see Figure 2 for definitions): P_hs, PpP_hs, and PpS_hs (or PsP_hs). The differential travel-time equations depend on *H*, V_P/V_S, the average crustal *P*-wave velocity ($\overline{V}_P$), and the ray parameter (*p*). We determine the ray parameter from the event depth and epicentral distance and use average crustal *P*-wave velocities of 6.2 and 6.4 km/s (Lin et al., 1993; Li and Mooney, 1998; Wang et al., 2003). At each station, we sum the amplitudes of the receiver functions at the predicted differential travel times of the *Ps*, *PpPs*, and *PpSs* (or *PsPs*) phases for a given *H* and V_P/V_S:

$$s(H, V_P/V_S) = \sum_N \left[a(t_{P-Ps}) + a(t_{P-PpPs}) + a(t_{P-PpSs}) \right], \quad (1)$$

where *N* is the number of receiver functions at each station and *a(t)* is the amplitude of a receiver function at time *t*. We perform a grid search in the V_P/V_S - *H* parameter space, and take the optimum solution to be at the maximum of the amplitude stack surface.

We use the 90% contour lines as an indication of uncertainty (Hetland et al., 2004). In an isotropic medium, the Poisson's ratio (ν) is given by:

$$\nu = \frac{1}{2}\left(1 - \frac{1}{(V_P/V_S)^2 - 1}\right). \quad (2)$$

The Poisson's ratio is an important parameter for determining crustal composition because it is sensitive to mineralogy (e.g., Christensen, 1996) and the presence of fractures, fluid content, and partial melt (e.g., O'Connell and Budiansky, 1974; Mavko, 1980). .

2.3 Least-squares inversion and velocity modeling

A least-squares inversion of receiver function waveforms is performed to estimate the crustal velocity structure (Ammon et al., 1990). This technique is more sensitive to velocity contrasts than to the absolute magnitude of the velocities, but it requires a starting velocity model that is close to the actual velocities (Owens et al., 1984; Ammon et al., 1990). Here, we accommodate this requirement by using the seismic refraction results of Zhu et al. (personal communication, 2003) as our starting velocity models. We invert for velocity structures consisting of horizontal layers with fixed thicknesses of 2 km, not because we expect to resolve such detail, but because the receiver functions are dominated by shear-converted phases with a typical wave length of ~8 km and layers as thin as 2 km may influence the inverse modeling. Furthermore, we fix the Poisson's ratios and Moho depths at the values derived from the slant-stacking method. We invert only for the *S*-wave velocity; the *P*-wave velocity is derived from these results in conjunction with the V_P/V_S ratio. Approximate densities (ρ) throughout the model are derived using the equation $\rho = 0.32\ V_P + 0.77$ (Berteussen, 1977).

The inversion seeks to minimize the difference between the observed and model-generated receiver function waveforms. A distribution of possible solutions is built by running the inversion for a range of starting models based on perturbations to the prescribed initial model (see Ammon et al., 1990), and the preferred solution is computed by averaging the solutions that fit the data within data uncertainty using a chi-squared test with 95% confidence (Lodge and Helffrich, 2006; see Appendix I for details). At each station, we apply varying levels of smoothing until we can model the dominant phases and avoid over-complexity in the resultant model.

Since the inversion tends to overfit the data and produce solutions that may contain too much structure, we proceed by simplifying the preferred crustal model to obtain a model that is more realistic and, therefore, easier to interpret (see, e.g., Lodge and Helffrich, 2006). Simplified models are constructed by investigating the effects of isolated portions of the least-squares solution on the receiver function waveform. Velocity gradient are replaced by single, sharp discontinuities, and adjacent model layers exhibiting similar velocities are grouped to form a coarser model. Once the minimum structure has been identified, the solution to this "simplified model" is found by performing a grid-search over its parameters and computing the average of all the models that fit the data within 95% confidence (Lodge and Helffrich, 2006; see Appendix I for details).

3. Data

We use data from a network of 25 temporary broadband seismometers operated by MIT and the Chengdu Institute of Geology and Mineral Resources (CIGMR) for one year between September 2003 and October 2004. The station distribution is shown in Figure

1. We analyze waveforms from seismic events that are selected based on the following criteria: (1) body-wave magnitude $m_b > 5.6$ to insure high signal-to-noise ratio, (2) epicentral distances (Δ) between 30º and 100º to avoid wavefield complexities due to upper mantle discontinuities or diffraction at the core-mantle boundary. In order to get relatively simple source functions, earthquakes with vertical waveforms containing two or more obvious pulses are avoided. In addition, data with poor signal-to-noise ratios are discarded. This includes, for example, data with no obvious first-*P* arrivals and/or large-amplitude surface waves in the observing time window.

With a deployment period of one year only, our array recorded data from a relatively narrow range of backazimuths. A total of 147 events, mostly from the circum-Pacific seismogenic belt (Figure 3), were used to produce 1329 individual receiver function waveforms. However, due to equipment failure, periods of high noise levels, and variable durations of station operation, only a subset of the total number of events were recorded at a particular station. In addition, we used data recorded between 1990–2002 at KMI (Kunming), a station of the China Digital Seismograph Network (CDSN). The number of events selected for analysis at each station is given in Table 1.

4. Results

4.1 Receiver functions from 25 temporary stations

At most stations, *P*-to-*S* conversions from the Moho are clearly identified on both individual and stacked receiver functions. Other prominent phases are observed after the direct *P* arrival, indicating the presence of significant intra-crustal structure. We illustrate our analysis with data from stations MC22 and MC05 (Figure 4).

Station MC22 (24.5°N; 100.2°E) was located in the Sanjiang tectonic unit, to the

south of the Red River fault. The 29 receiver functions obtained for this station are plotted in Figure 4a, for backazimuths between 8° and 253°. Visual inspection reveals a clear P_ms arrival at ~5 s on all 29 radial receiver functions. Subsequent arrivals include a strong positive one at ~16 s and a weak negative one at ~22 s (Figure 4a). Based on their polarity and relative arrival time, these arrivals could be the free-surface multiples of the Moho, i.e., PpP_ms and PpS_ms (or PsP_ms) phases, respectively (see Figure 2). In some receiver functions, positive arrivals observed between 9–11 s may correspond to *P*-to-*S* conversions from upper mantle discontinuities or multiples from intra-crustal discontinuities. Since there are no obvious phases corresponding to *P*-to-*S* conversions from an intra-crustal discontinuity, we interpret the arrivals at 9–11 s as *P*-to-*S* conversions from structure in the upper mantle (~80 km). The positive arrival at ~7 s in the transverse receiver function (thin blue line in Figure 4b) is likely due to *P*-to-*S* conversion from an anisotropic and/or tilted layer, either in the mantle (direct arrival) or in the crust (multiple). There are no prominent phases observed before P_ms (i.e., 5 s) in the transverse receiver function, which indicates that there are no significant effects of anisotropy or tilted layers at shallow depth (Zhang et al., 1995; Savage, 1998), which – in turn – implies that our assumption of a 1-D crustal velocity structure is adequate.

Station MC05 was located at (30.0°N; 100.2°E), which is in the Songpan-Ganze fold zone. Figure 4c and d show the processed receiver functions at this station. The initial *P*-wave pulse is time shifted by ~0.2 s. Such shifts, which have also been observed elsewhere (see, e.g., van der Meijde et al., 2003), can be attributed to the presence of a low-velocity layer near the surface (i.e., sediments) directly below the station. The

arrivals at ~5 and ~7–8 s may correspond to *P*-to-*S* conversions from intra-crustal and Moho discontinuities, respectively. Stacking events over all backazimuths can produce slightly broader peaks for P_ms and its multiple phases because of the dependence of the arrival time on backazimuth. Therefore, we stack 42 events from back azimuth range of 104.5°–156.7° (Figure 4d). For the same reason we bin events for stations MC06, MC11, and KMI (see Table 1). The small-amplitude phases that arrive before the P_ms phases represent *P*-to-*S* conversions within the crust. There is a clear positive phase at ~23 s, corresponding to the arrival of PpP_ms, and a negative phase at ~30 s, which corresponds to PpS_ms (or PsP_ms) (Figure 4c). No prominent phase appears on the transverse receiver function of station MC05 (Figure 4d).

In contrast to stations MC22 and MC05, some stations have no strong crustal P_ms conversions (Figure 5). The observation of time delays of the first pulse in receiver functions at most stations indicate that a near-surface low-velocity layer is widely distributed in our study area. The first pulses are complicated due to interference with *P*-to-*S* conversions from the bottom of the surface layers, which arrive within ~2 s after the first pulse, e.g., MC02 and MC11 (Figure 5). At station MC03, which is located just east of the Longmen Shan fault, the radial receiver function waveform has several low-amplitude, positive phases within ~10 s after the first-*P* arrival. The 10.2-s phase is most probably the P_ms phase because it does not depend on backazimuth and because it is consistent with a Moho depth of ~60 km inferred from refraction studies (Zhu et al., 2003, personal communication), which corresponds to a P_ms phase at > 7.0 s assuming an average crustal velocity $V_P < 6.8$ km/s and a Poisson's ratio ≥ 0.25. At station KMI, which is located near N-S trending strike-slip faults (Figure 1), large-amplitude positive

phases are observed at ~5 s after the main pulse, which could be P_ms. The large variation in the radial receiver functions with backazimuth indicates a laterally heterogeneous structure beneath station KMI.

4.2 Slant-stacking

We classify stations into three categories depending on the reliability of the derived crustal properties. The first category corresponds to stations for which the P_ms and PpP_ms phases are clearly visible in the radial receiver functions, and for which a clear maximum in the V_P/V_S vs. H diagram can be observed even if phase identification is difficult. The second category corresponds to stations with multiple maxima in the V_P/V_S vs. H diagram. When identification in the stacks of the maxima corresponding to Moho is ambiguous we use independent estimates of crustal thickness (Wang et al., 2003; Zhu et al, personal communication, 2003) and restrict the average crustal Poisson's ratio to reasonable values (~0.25–0.30). The third category corresponds to stations for which the records are too complex or too noisy to determine V_P/V_S and H with sufficient confidence. In this study, we only use stations in the first two categories for further S-wave velocity analysis (Table 1).

Figure 6a-b shows the slant-stacking results from station MC22. The following phases are visible: the P_ms phase at ~5 s after the first-P arrival, the PpP_ms phase at ~16 s, and (more tentatively) the PpS_ms (or PsP_ms) phases at ~22 s. Travel time curves of these phases (thick lines in Figure 6a) are derived using the combination of H and V_P/V_S that gives the maximum amplitude of the stack. There is only one global maximum in the V_P/V_S vs. H diagram, which corresponds to the optimum solution. Therefore, this

station is classified in the first category. We obtain a crustal thickness of 37.5 ± 1.5 km and an average crustal Poisson's ratio of 0.25 ± 0.04 beneath this station (Figure 6b). The inferred crustal thickness of 37.5 km is slightly less than the values of 43 and 41.3 km from previous studies (Wang et al., 2003; Zhu et al., personal communication, 2003; see Table 1). The receiver function study using data from the Yunnan regional seismic network (Hu et al., 2003) yielded a crustal thickness of 36.0±1.0 km at nearby station YX (24.3°N, 100.1°E). Hu et al. (2003) also derived a Poisson's ratio of 0.31±0.01, which is larger than but not incompatible with our estimate of 0.25±0.04.

Station MC05 has local maxima in addition to a global maximum in the V_P/V_S -H diagram (Figure 6c-d). One of the local maxima yields H = 42.5 km and Poisson's ratio of 0.33, whereas the global maximum corresponds to a crustal thickness of 59.0 ± 1.0 km and average crustal Poisson's ratio of 0.26 ± 0.01. Because seismic refraction data suggest a thickness of ~62.5 km (Zhu, personal communication, 2003) we select the latter values for crustal thickness (i.e., 59.0 ± 1.0 km) and Poisson's ratio (i.e., ~0.26) at station MC05.

The receiver function waveforms from stations MC12, MC18, and MC19 are too noisy to identify the P_ms phase among several pulses with similar amplitude (Figure 5). They are in the third category and thus not included in further analysis.

The slant-stacking analysis reveals that the depth to the Moho changes gradually across our array, from ~37 km in Yunnan province to ~64 km below eastern Tibet. The average crustal Poisson's ratio varies between 0.21 and 0.32 and is the lowest in the southern Yangtze platform. The Poisson's ratio is highest, with values consistently

above 0.30, below the eastern margin of the Tibetan plateau just west of the Sichuan basin (below the latter the Poisson's ratios are generally less than 0.29). The Songpan-Ganze fold zone, the region of high average elevation (~4 km), has a thick crust. Station MC01, situated between the Xianshuihe and Longmen Shan faults, has the thickest crust (i.e., 64 km ± 1.0 km) and a small Poisson's ratio (i.e., 0.21 ± 0.1). On the Yangtze platform, MC02 and MC10 sample the western Sichuan basin (Figure 1). Here the crust thickness is between ~46 and 41 km, and the Poisson's ratios between ~0.26 and 0.29. The crust-mantle boundary of the Yangtze platform deepens northwestward from ~40 km to 56 km. The Poisson's ratio generally decreases eastward from ~0.30 to 0.22. The Sanjiang fold zone, west of the Red River fault, has a crustal thickness of ~38–46 km and Poisson's ratio of ~0.23–0.25.

4.3 *S*-wave velocity profiles

S-wave velocity profiles derived from least-squares inversion and grid search through simplified models are show in Figure 7 (for 8 stations) and in Figure A11, Appendix II (all stations). Low-velocity zones are identified as velocity minima on smoothed crustal velocity models beneath many stations in the southeastern part of the Tibetan plateau. The thickness of near-surface low-velocity layers (S-LVL) varies from ~0 to 10 km. An intra-crustal low-velocity layer (IC-LVZ) is mostly observed in the Songpan-Ganze fold zone and the western Yangtze platform. On average, the *S*-wave velocity in the IC-LVZ is ~0.5–0.8 km/s lower than that of its overlying layer. Both S-LVL and IC-LVZ are robust features: S-LVLs are well constrained by a ~0.2 s time shift of the incident *P*-wave pulse; IC-LVZs are only assigned to stations where a

low-velocity layer is required both in the least-squares solution and in the simplified model to fit the measured receiver function waveform (see Appendix I).

4.3.1 Songpan-Ganze fold zone (SG)

At MC01, the receiver functions synthesized from the derived *S*-wave velocity profiles match the observed data within the observational uncertainty (Figure 7). The 68-km thick crust has a 20-km thick upper crust with *S*-wave velocity of ~3.7 km/s and a 30-km lower crust with *S*-wave velocity of 3.9 km/s. There is a low-velocity zone at ~20-40 km which is necessary to explain the negative arrival at ~2.6 s in the receiver function waveform. Our results are consistent with previous *S*-wave tomography, which yielded a small negative velocity anomaly at ~50 km beneath this station (Wang et al., 2003). MC04 and MC08 have similar velocity structures: there are no obvious low-velocity layers near the surface and the *S*-wave velocities in the upper and middle crust are more or less constant. The 57-km thick crust at MC04 consists a ~32-km upper crust with *S*-wave velocity of 3.2 km/s and 25-km lower crust with *S*-wave velocity of 3.5 km/s.

Stations MC05-07 have very similar *S*-wave velocity profiles. These stations are marked by an IC-LVZ with S-wave velocity of ~3.3 km/s. The IC-LVZ extends between ~15 and 38 km depth at station MC05 (Figure 7), which is necessary to explain the negative phases at ~2 s and 6 s in the receiver function waveform (see Appendix I). In the same region, MT studies show a high conductive layer below ~10 km (Sun et al., 2003), and *S*-wave tomography shows a low-velocity anomaly between ~10–30 km depth (Wang et al., 2003). The positive velocity gradient at ~30 km corresponds to the 5-s arrival in the receiver function waveform, which can be related to the Conrad

discontinuity (i.e., ~25 km depth) inferred from deep seismic sounding (Wang et al., 2003). We note that the strong Moho multiples that appear near ~23 s and ~31 s in the synthetic waveforms calculated from the preferred velocity model are not as clearly visible in the stacked receiver functions (Figure 7). This discrepancy is due, in large part; to the fact that receiver functions are stacked using moveout curves that account for variations in relative travel time of direct conversions, but that do not stack multiples coherently.

4.3.2 Yangtze platform (YZ)

Two stations sample the crust of the western Sichuan basin. Beneath station MC02, the S-LVL is ~5 km thick, which is consistent with the layers of Mesozoic sediments in the Sichuan basin (Kirby et al., 2000). The crust there has a thickness of 48 km and exhibits a fairly uniform *S*-wave velocity (average ~3.7 km/s) below the S-LVL. In contrast, station MC10 has an IC-LVZ at ~10-20 km with *S*-wave velocity of ~3.1 km/s.

In the western Yangtze platform, stations MC17, MC20, and MC23 have similar *S*-wave velocity profiles, without obvious IC-LVZs. Stations MC13 and MC15 have IC-LVZs with *S*-wave velocities ~3.1 km/s. A similar IC-LVZ had been inferred from other receiver function studies (Hu et al., 2003; He et al., 2004), except for a station at (26.9°N, 100.2°E), which is close to MC15, where an IC-LVZ has not been previously observed (Hu et al., 2003). Stations MC03, MC09, MC11, MC16, MC25, and MC24 sample the Yangtze platform from north to south. Their *S*-wave velocity profiles are significantly different. Station MC03, located near the Longmen Shan fault, reveals an IC-LVZ at ~20–44 km and two velocity discontinues at ~44 km and 64 km

(corresponding to the arrivals at ~5.2 and 10.1 s in the receiver function waveform). These can be interpreted as intracrustal and Moho discontinuities, respectively. Station MC09 has an IC-LVZ at ~15–30 km, with an *S*-wave velocity of ~3.2 km/s. Stations on the southern Yangtze platform do not show evidence for IC-LVZs. Our results generally agree with previous receiver function studies in southern Tibet (Hu et al., 2003; He et al., 2004).

4.3.3 Sanjiang fold system (SJ)

Stations MC21 and MC22 sample the Sanjiang fold system, west of the Red River fault. MC21 is located to the east of the Tengchong volcanic area. The crust deepens northward by ~9 km from station MC22 to station MC21. There is no obvious IC-LVZ and intracrustal discontinuities at both stations. Similar receiver function results were observed by Hu et al. (2003) in the Sanjiang fold system.

5. Discussion

5.1 Crustal thickness

The crustal thickness varies between 37 and 64 km in SE Tibet and its surrounding area (Figure 8). The thickness of the crust is large beneath the Songpan-Ganze fold zone (~60 km) and decreases eastward to the western Sichuan basin (~46 km) and southeastward to the Yangtze platform (~40 km). The crust beneath the Sanjiang fold zone has a thickness of ~38-46 km.

In general, the Moho depths derived in our study are consistent with previous results (e.g., Li and Mooney, 1998; Hu et al., 2003; Wang et al., 2003; He et al., 2004). Specifically, Figure 9 (also Table 1) shows that for realistic values of the average crustal *P*-wave velocity (6.2–6.4 km/s) our results agree well with estimates from seismic

refraction profiles (Zhu et al., personal communication, 2003) or Bouguer gravity anomaly and deep seismic sounding profiles data (Wang et al., 2003). The correlation coefficients between our Moho depth values and their estimates are 0.88 and 0.86, respectively. The only significant outliers are stations MC01 and MC03, for which we obtained thicker crust (Table 1). When we include these outliers, the root mean square of the differences between our results and those from the independent studies are about 4 km. Some of this difference can be due to the fact that the receiver function analysis and the seismic refraction study sample the crust at different locations and that the spatial resolution of two methods is different (Chevrot and van der Hilst, 2000).

Figure 10 shows *S*-velocity profiles along an east-west cross section (line 1 in Figure 1) beneath the northern part of our study region, adjacent to the Sichuan basin; the topographic slope across the east margin of the Tibetan plateau (Figure 10, top) is steep and the elevation decreases by ~3500 m over a lateral distance of 150 km. The steep topographic gradient in the western Sichuan basin was interpreted by Clark et al. (2005) to be a result of crustal material flowing around the strong lithosphere of the Sichuan block in the channel flow model. From station MC05 – on the plateau proper – to station MC02 – in Sichuan basin – the base of the crust shallows by 9.5 ± 2.0 km and the elevation decreases by ~3500 m. An Airy isostastic model predicts a change in crustal thickness of ~24 km (Braitenberg et al., 2000), which suggests that crustal material may still be piling up at the east margin of the Tibetan plateau. Along Line 2 (Figure 11), which transects the southeastern margin of the Tibetan plateau, the average topographic slope is smaller than across the eastern margin (line 1). The crust shallows southeastward by 19.7 ± 6.0 km with a change in elevation of ~2300 m, in agreement

with an Airy isostatic model. Our result of Moho compensation using the Airy isostastic model (Braitenberg et al., 2000) is consistent with previous gravity anomaly studies, which indicated that the topography of the southeastern part of the Tibetan plateau is locally compensated except for the eastern margin across the Longmen Shan fault on to the western Sichuan basin (Jiang and Jin, 2005; Jordan and Watts, 2005).

5.2 Poisson's ratio and (average) crustal composition

Poisson's ratios can help constrain crustal mineralogy and chemical composition. Mineral physics and field constraints indicate that (1) the Poisson's ratio increases more-or-less linearly with decreasing SiO_2 content for continental crust, and (2) high ratios (> 0.30) suggest the existence of partial melt (Christensen, 1996; Owens and Zandt, 1997), especially if the perturbation in Poisson's ratio is localized to an intra-crustal layer (see Appendix III). We interpret the large range of observed Poisson's ratio (0.22–0.32) in the southeastern part of the Tibetan plateau to be a result of heterogeneity in crustal composition and, locally, the existence of partial melt.

Most of our study region has an intermediate-to-high Poisson's ratio (> 0.25) except for a few stations in the southern Yangtze platform. The ratio is highest (> 0.30) in the eastern margin of the Tibetan plateau, just west of the Sichuan basin (Figure 8). In the Yangtze platform, Poisson's ratios generally decrease eastward, from ~0.30 to 0.22. The normal-to-high values in the western Yangtze platform (~0.26-0.30) are consistent with a mafic/ultramafic lower crust as inferred from recent geophysical surveys (Xu et al., 2001), and may indicate the presence of partial melt in the crust, whereas low-to-intermediate values suggest a felsic-to-intermediate composition in the southern Yangtze platform. The ratios in the Sanjiang fold system (~0.23–0.25) are consistent with

457 results from seismic refraction studies and suggest an "average" crustal composition (Kan
458 et al., 1986; Li and Mooney, 1998).

459 Hu et al. (2003) estimated Poisson's ratios – using equations (1) and (2) – from
460 differential travel times of P_ms and PpP_ms phases at 23 temporary stations in Yunnan
461 province. They showed that the western Yangtze platform has Poisson's ratios of
462 0.30–0.35, which are higher than our values of 0.26–0.30. This discrepancy may, in
463 part, be due to differences in data and methodology. Our results are consistent with
464 Zurek et al. (personal communication, 2007), who used a slant-stacking method similar to
465 the one deployed here.

466 **5.3 Low-velocity zones**

467 Our results suggest the presence of complex 3-D heterogeneity in the crust beneath
468 SE Tibet. The most prominent features in the *S*-wave velocity profiles presented here
469 are the near-surface and intra-crustal low-velocity zones (Figure 7, 10, and 11). The
470 quasi-ubiquitous S-LVL can be related to the surface sedimentary basins (Leloup et al.,
471 1995; Song and Lou, 1995; Burchfiel and Wang, 2003). The IC-LVZ is widely
472 observed in the study region, but with significant lateral variation in its depth and
473 strength. In some places the IC-LVZ corresponds to the middle crust, but in other
474 places it marks the lower crust. In general, it becomes thinner toward the Sichuan basin
475 and is absent in the southern part of the Yangtze platform (Figure 8). Compared to the
476 shallow crust, the reduction of the *S*-wavespeed in IC-LVZ is in the range of ~12–19%.

477 The existence of IC-LVZs as inferred here is generally consistent with results from
478 seismic sounding, seismic tomography, and previous receiver function analyses (e.g., Li
479 and Mooney, 1998; Huang et al., 2002; Wang et al., 2003; Hu et al., 2003; He et al., 2004;

Yao et al., 2007). Along line 1 (Figure 10), the IC-LVZ also coincides with one or more intra-crust layers of high (electric) conductivity inferred from MT data (Sun et al., 2003).

5.4 Partial melt?

Earthquake focal depths and heat flow studies both indicate a relatively high geothermal gradient in the southeastern part of the Tibetan plateau (Sun et al., 2004; Wu et al., 1988; Hu et al., 2000). In crystalline continental crust, seismic velocities generally increase with increasing depth. However, wavespeed reductions can occur in regions with steep geothermal gradients (e.g., Kern and Richter, 1981; Kono et al., 2006) and, in particular, in regions of partial melt (Meissner, 1986). In view of (i) the magnitude of the reduction in shear wavespeed in the IC-LVZs, (ii) the high average Poisson's ratios of the crust and their possible translation into vertically localized perturbations (see Appendix III) , (iii) the correlation with a zone of high conductivity inferred from the inversion of MT data, and (iv) the association with high heat flow, we suggest that crustal partial melt exists beneath parts of the eastern margin of the Tibetan plateau, possibly with continuation into the northwesternmost part of the Yangtze platform.

In general, the *S*-wave velocity decreases and Poisson's ratio increases drastically when the temperature approaches and exceeds the solidus. Mueller and Massonne (2001) suggested that for typical mid-crustal pressures, granite starts to melt at ~650°C. If we suppose a similar composition, the inferred Poisson's ratio > 0.30 and *S*-wave velocities of ~3.0–3.2 km/s in the IC-LVZs (~10–30 km in depth) indicate a temperature of ~700–800°C and an amount of melt less than 4%. This interpretation is consistent with inferences from receiver function studies in northern Tibet (Zhu et al., 1995) and

with Roger et al. (1995), who suggested that the young Konga Shan granite (~10 Ma) at the southern segment of the Xianshuihe fault (Figure 1) may have originated from partial melting of continental crust. However, our results suggest that partial melt is restricted to certain geographical regions (that is, the data do not require it for large parts of our study region) and that it involves the middle or the lower crust, and perhaps, in some locations, both (see also, Yao et al., 2007).

Previous geological and experimental studies (Leloup et al., 1995; Rabinowicz and Vigneresse, 2004) suggested that crustal partial melt may be partly due to shear heating in southeastern Tibet. Another contribution may come from the upper-mantle decompression melting which also contributed to the young volcanism (Wang et al., 2001). Intra-crustal zones of partial melt in northern Tibet have been attributed to the extrusion of mantle-derived magma (e.g., Zhu et al., 1995; Nelson et al., 1996; Kind et al., 2002). Furthermore, a shallow IC-LVZ (~10–20 km) around the Tengchong volcano was interpreted by Wang and Gang (2004) to be the result of upper-mantle magma activity and heat conduction through the near vertical fault.

Since the viscosity of crustal rocks decreases with increasing fraction of partial melt (Bagdassarov and Dorfman, 1998), it is tempting to associate the IC-LVZ with a mechanically weak zone. This would be consistent with a model in which crustal shortening is accommodated by channel flow in the mid-to-lower crust (Royden et al., 1997; Clark and Royden, 2000; Roy and Royden, 2000a and b; Clark et al., 2005). Insofar as the association of IC-LVZs with layers of weaker rheology is correct, the results from receiver function analysis (this study) and from surface wave array tomography (Yao et al., 2007) suggest that there is substantial lateral variation in

existence, strength, and position (e.g., depth range) of such zones. In turn, this suggests a complex 3-D geometry of intra-crustal channel flow.

6. Summary

By analyzing receiver functions from 25 temporary seismograph stations, we estimated the crustal velocity structure in the southeastern margin of the Tibetan plateau. The crust varies in thickness from ~60 km in the Songpan-Ganze fold system to ~40 km in the southern Yangtze platform. The gradient of the Moho discontinuity is the greatest in the eastern margin of Tibet toward the western Sichuan basin. The crustal thickness generally follows the Airy isostatic model except toward the western Sichuan basin, which indicates that crustal material may still be piling up at the eastern margin of the Tibetan plateau. Poisson's ratio varies greatly in our study region. The western Yangtze platform exhibits intermediate-to-high Poisson's ratios (> 0.30), which can be related to the existence of high-velocity lower crust with a mafic/ultramafic composition and, locally, to the presence of partial melt. In general, the overall crustal chemical composition varies between felsic and intermediate.

Arguably the most conspicuous features in the velocity profiles derived here are the pronounced low-velocity zones in the crust. The geometry may not be well resolved, but these IC-LVZs are required by the data (the starting models used for the inversions do not have clear low-velocity structures in the crust (Figure 7)). An IC-LVZ is widely observed in the study region, but with significant lateral variation in its depth and strength. It becomes thinner toward the Sichuan basin and is absent in the southern part of the Yangtze platform (Figure 8). The *S*-wavespeed reduction in IC-LVZ is ~12–19% relative to the shallow crust. As seismic velocities generally increase with increasing

549 depth in crystalline continental crust, we infer the possible existence of crustal partial
550 melt in IC-LVZ. Our interpretation is supported by observations of crustal
551 high-conductivity layers and high heat flow values in our study area (e.g., Wang and
552 Huang, 1988; Hu et al., 2000; Sun et al., 2003) and by inferences from high-resolution
553 surface wave tomography (Yao et al., 2007). Collectively, these observations indicate
554 that the low-viscosity zone in the crust of the central Tibetan plateau probably extends
555 into southeastern Tibet. The substantial lateral variations in the existence, character,
556 strength, and position of IC-LVZ may point to intra-crustal channel flow but with a
557 complex 3D geometry.

558 **References:**

559 Ammon, C., Randall, G., and Zandt, G., 1990. On the non-uniqueness of receiver
560 function inversions. J. Geophys. Res., 95: 15303-15318.
561 Avouac, J.P., and Tapponnier, P., 1993. Kinetic model of active deformation in
562 central-Asia. Geophys. Res. Lett., 20: 895-898.
563 Bagdassarov, N., and Dorfman, A., 1998. Granite rheology: magma flow and melt
564 migration. J. Geol. Soc., 155: 863-872.
565 Berteussen, K.A., Moho depth determinations based on spectral ratio analysis of
566 NORSAR long-period P waves, Phys. Earth Planet. Inter., 31: 313-326, 1977.
567 Bostock, M.G., 1998. Mantle stratigraphy and evolution of the Slave Province. J
568 Geophys. Res., 103: 21183-21200.
569 Braitenberg, C., Zadro, M., Fang, J., Wang, Y., and Hsu, H.T., 2000. The gravity and
570 isostatic Moho undulations in Qinghai-Tibet plateau, J. Geodyn., 30 (5): 489-505.

571 Burchfiel, B.C., and Wang, E.C., 2003. Northwest-trending, middle Cenozoic,
572 left-lateral faults in southern Yunnan, China, and their tectonic significance. J.
573 Strut. Geol., 25 (5): 781-792.
574 Burchfiel, B.C., Chen, Z., Liu, Y., and Royden, L.H., 1995. Tectonics of the
575 Longmenshan and adjacent regions, central China. Inter. Geol. Rev., 37
576 (8):661-735.
577 Chen, B.W., Wang, K.W., and Liu, W.X., 1987. Geotectonics in
578 Nujiang-Lancangjiang-Jinshajiang Region (in Chinese). Geol. Publ., Beijing, 204
579 pp.
580 Chen, Z., Burchfiel, B.C., Liu, Y., King, R.W., Royden, L.H., Tang, W., Wang, E.,
581 Zhao, J., and Zhang, X., 2000. Global Positioning System measurements from
582 eastern Tibet and their implications for India/Eurasia intercontinental deformation.
583 J. Geophys. Res., 105(B7): 16215-16227.
584 Chevrot, S., and van der Hilst, R.D., 2000. The Poisson ratio of the Australian crust:
585 geological and geophysical implications. Earth Planet. Sci. Lett., 183 (1-2):
586 121-132.
587 Christensen, N.I., 1996. Poisson's ratio and crustal seismology. J. Geophys. Res., 101
588 (B2): 3139-3156.
589 Clark, M.K., and Royden, L.H., 2000. Topographic ooze: building the eastern margin
590 of Tibet by lower crustal flow. Geology, 28 (8): 703-706.
591 Clark, M.K., Bush, J.W.M., and Royden, L.H., 2005. Dynamic topography produced
592 by lower crustal flow against rheological strength heterogeneities bordering the
593 Tibetan Plateau. Geophy. J. Int., 162: 575-590.

Flesch, L.M., Holt, W.E., Silver, P.G., Stephenson, M., Wang, C.Y., and Chan, W.W., 2005. Constraining the extent of crust-mantle coupling in central Asia using GPS, geologic, and shear-wave splitting data. Earth Planet. Sci. Lett., 238 (1-2): 248-268.

Frederiksen, A.W., Folsom, H., and Zandt, G., 2003. Neighbourhood inversion of teleseismic Ps conversions for anisotropy and layer dip. 155 (1): 200-212.

Gurrola, H., Baker, G.E., and Minster, J.B., 1995. Simultaneous time-domain deconvolution with application to the computer of receiver functions. Geophys. J. Int., 120: 537-543.

He, Z.Q., Ye, T.L., and Su W., 2004. S-wave velocity structure of the middle and upper crust in the Yunnan region, Chinese (in Chinese). J. Geophys., 47 (5): 838-844.

Hetland, E.A., Wu, F.T., and Song, J.L., 2004. Crustal structure in the Changbaishan volcanic area, China, determined by modeling receiver function. Tectonophysics, 386: 157-175.

Holt, W.E., 2000. Correlated crust and mantle strain fields in Tibet. Geology, 28 (1): 67-70.

Hu, J.F., Su, Y.J., Zhu, X.G., and Chen, Y., 2003. S-wave velocity and Poisson's ratio structure of crust in Yunnan and its implication (in Chinese). Sci. China, Ser. B, 48 (2): 210-218.

Hu, S.B., He, L.J., and Wang, J.Y., 2000. Heat flow in the continental area of China: a new data set. Earth Planet. Sci. Lett., (2): 407-419.

Huang, J.L., Zhao, D.P., and Zheng, S.H., 2002. Lithospheric structure and its relationship to seismic and volcanic activity in southwest China. J. Geophys. Res., 107 (B10), 2255, doi: 10.1029/2000JB0000137.

Jiang, X.D., and Jin, Y., 2005. Mapping the deep lithospheric structure beneath the eastern margin of the Tibetan Plateau from gravity anomalies. J. Geophys. Res., 110, B07407, doi: 10.1029/2004JB003394.

Jordan, T.A., and Watts, A.B., 2005. Gravity anomalies, flexure and the elastic thickness structure of the India-Eurasia collisional system. Earth Planet. Sci. Lett., 236 (3-4): 732-750.

Kan, R.J., Hu, H.X., Zeng, R.S., Mooney, W.D., and McEvilly, T.V., 1986. Crustal structure of Yunnan province, Peoples-Republic-of-China, from seismic refraction profiles. Science, 234(4775): 433-437.

Kern, H., and Richter, A.E., 1981. Temperature derivates of compressional and shear wave velocities in crustal and mantle rocks at 6 Kbar confining pressure. J. Geophys., 49 (1): 47-56.

Kind, R., Kosarev, G.L., and Petersen, N.V., 1995. Receiver functions at the stations of the German regional seismic network (GRSN). Geophys. J. Int., 121 (1): 191-202.

Kind, R., Ni, J.F., Zhao, W.J., Wu, J.X., Yuan, X.H., Zhao, L.S., Sandvol, E., Reese, C., Nabelek, J., and Hearn, T., 1996. Evidence from earthquake data for a partially molten crustal layer in southern Tibet. Science, 274: 1692-1694.

637 Kind, R., Yuan, X., Saul. J., Nelson, D., Sobolev, S.V., Mechie, J., Zhao, W., Kosarev,
638 G., Ni, J., Achauer, U., Jiang, M., 2002. Seismic images of crust and upper mantle
639 beneath Tibet: evidence for Eurasian plate subduction. Science, 298: 1219-1221.
640 King, R.W., Shen, F., Burchfiel, B.C., Royden, L.H., Wang, E., Chen, Z., Liu, Y.,
641 Zhang, X.Y., Zhao, J.X., and Li, Y., 1997. Geodetic measurement of crustal
642 motion in southwest china. Geology, 25: 179-182.
643 Kirby, E., Whipple, K.X., Burchfiel, B.C., Tang, W.Q., Berger, G., Sun, Z.M., and
644 Chen, Z.L., 2000. Neotectonics of the Min Shan, China: Implications for
645 mechanisms driving Quaternary deformation along the eastern margin of the
646 Tibetan Plateau. Geol. Soc. Am. Bull., 112 (3): 375-393.
647 Kono, Y., Ishikawa, M., Arima, M., 2006. Laboratory measurements of P- and S-wave
648 velocities in polycrystalline plagioclase and gabbronorite up to 700°C and 1 GPa:
649 Implications for the low velocity anomaly in the lower crust. Geophys. Res. Lett.,
650 33, L15314, doi: 10.1029/2006GL026526.
651 Langston, C.A., 1979. Structure under Mount Rainier, Washington, inferred from
652 teleseismic body waves. J. Geophys. Res., 84: 4749-4762.
653 Leloup, P.H., Lacassin, R., Tapponnier, P., Schärer, U., Zhong, D.L., Liu, X.H., Zhang,
654 L.S., Ji, S.C., and Trinh, P.T., 1995. The Ailao Shan-Red River shear zone
655 (Yunnan, China), Tertiary transform boundary of Indochina. Tectonophysics, 251:
656 3-84.
657 Lev, E., Long, M.D., and van der Hilst, R.D., 2006. Seismic Anisotropy in Eastern
658 Tibet from shear-wave splitting reveals changes in lithospheric deformation. Earth
659 Planet. Sci. Lett., 251 (3-4): 293:304.

660 Li, S., and Mooney, W.D., 1998. Crustal structure of China from deep seismic
661 sounding profile. Tectonophysics, 288: 105-113.
662 Lin, Z., Hu, H., and Zhang, W., 1993. The preliminary interpretation of deep seismic
663 sounding in western Yunnan (in Chinese). Acta Seismol. Sin., 15 (4): 282-295.
664 Lodge, A., and Helffrich, G., 2006. Depleted well root beneath the Cape Verde Islands,
665 Geology, 34 (6): 449-452
666 Mavko, G.M., 1980. Velocity and attenuation in partially molten rocks. Geophys. J.
667 Int., 85: 5173-5189.
668 McNamara, D.E., Owens, T.J., Silver, P.G., and Wu, F.T., 1994. Shear wave
669 anisotropy beneath the Tibetan Plateau. J. Geophys. Res., 99 (B7): 13655-13665.
670 Meissner, R., 1986. The continental crust; a geophysical approach. Int. Geophys. Ser.,
671 34: 426 pp.
672 Molnar, P., and Tapponnier, P., 1975. Cenozoic tectonics of Asia: Effect of a
673 continental collision. Science, 189: 419-426.
674 Mueller, H.J., and Massonne, H.J., 2001. Experimental high pressure investigation of
675 partial melting in natural rocks and their influence on V_P and V_S. Phy. Chem.
676 Earth (A), 26 (4-5): 325-332.
677 Nelson, K.D., Zhao, W.J., Brown, L.D., Kuo, J., Che, J.K., Liu, X.W., Klemperer,
678 S.L., Makovsky, Y., Meissner, R., Mechie, J., Kind, R., Wenzel, F., Ni, J.,
679 Nabelek, J., Chen, L.S., Tan, H.D., Wei, W.B., Jones, A.G., Booker, J., Unsworth,
680 M., Kidd, W.S.F., Hauck, M., Alsdorf, D., Ross, A., Cogan, M., Wu, C.D.,
681 Sandvol, E., and Edwards, M., 1996. Partially molten middle crust beneath
682 southern Tibet; synthesis of Project INDEPTH results. Science, 274: 1684-1688.

O'Connell, R.J. and Budiansky, B., 1974. Seismic velocities in dry and saturated cracked solids. J. Geophys. Res., 79: 5412-5426.

Owens, T.J., Zandt, G., and Taylor, S.R., 1984. Seismic evidence for an ancient rift beneath the Cumberland Plateau, Tennessee; a detailed analysis of broadband teleseismic P-waveforms. J. Geophys. Res., 89: 7783-7795.

Owens, T.J., and Zandt, G., 1997. Implications of crustal property variations for models of Tibetan Plateau evolution. Nature, 387: 37-43.

Ozacar, A.A., and Zandt, G., 2004. Crustal seismic anisotropy in central Tibet: Implications for deformational style and flow in the crust. Geophys. Res. Lett., 31, L23601, doi: 10.1029/2004GL021096.

Rabinowicz, M., and Vigneresse, J.L., 2004. Melt segregation under compaction and shear channeling: Application to granitic magma segregation in a continental crust. J. Geophys. Res., 109, B04407, doi:10.1029/2002JB002372.

Roger, F., Calassou, S., Lancelot, J., Malavieille, J., Mattauer, M., Xu, Z.Q., Hao, Z.W., and Hou, L.W., 1995. Miocene emplacement and deformation of the Konga Shan granite (Xianshui He fault zone, west Sichuan, China): Geodynamic implications. Earth Planet. Sci. Lett., 130 (1-4): 201-216.

Rowley, D.B., 1996. Age of initiation of collision between India and Asia: A review of stratigraphic data. Earth Planet. Sci. Lett., 145: 1-13.

Roy, M., and Royden, L.H., 2000. Crustal rheology and faulting at strike-slip plate boundaries 1. An analytic model. J. Geophy. Res., 105 (B3): 5583-5597.

Roy, M., and Royden, L.H., 2000. Crustal rheology and faulting at strike-slip plate boundaries 2. Effects of lower crustal flow, J. Geophy. Res., 105 (B3): 5599-5613.

Royden, L.H., Burchfiel, B.C., King, R.W., Wang, E., Chen, Z.L., Shen, F., and Liu, Y.P., 1997. Surface deformation and lower crustal flow in eastern Tibet. Science, 276 (5313): 788-790.

Sandvol, E., Ni, J., Kind, R., and Zhao, W.J., 1997. Seismic anisotropy beneath the southern Himalayas-Tibet collision zone. J. Geophys. Res., 102(B8): 17813-17823.

Savage, M.K., 1998. Lower crust anisotropy or dipping boundaries? Effect on receiver function and a case study in New Zealand. J. Geophys. Res., 103 (B7): 15069-15087.

Silver, P.G., 1996. Seismic anisotropy beneath the continents: Probing the depths of geology. Ann. Rev. Earth Planet. Sci., 24: 385-&.

Song, H.B., and Lou, Z.L., 1995. The study of the basement and deep geological structures of Sichuan Basin. Earth Sci. Frontier (3-4): 231-237.

Sun, J., Jin, G.W., Bai, D.H., and Wang, L.F., 2003. Sounding of electrical structure of the crust and upper mantle along the eastern border of Qinghai-Tibet Plateau and its tectonic significance. Sci. China, Ser. D, 46: 243+Suppl.

Sun, Y.S., Kuleli, S., Morgan, F.D., Rodi, W., and Toksoz, M.N., 2004. Location Robustness of Earthquakes in Sichuan Province, China. Seism. Res. Lett., 75 (1), 55-62.

van der Meijde, M., van der Lee, S., Giardini, D., 2003. Crustal structure beneath broad-band seismic stations in the Mediterranean region. Geophy. J. Int., 152:729-739

Wang, C.Y., Chan, W.W., and Mooney, W.D., 2003. Three-dimentional velocity structure of crust and upper mantle in southeastern China and its tectonic implications. J. Geophys. Res., 108 (B9), 2442, doi:10.1029/2002JB001973.

Wang, C.Y., and Gang, H.F., 2004. Crustal structure in Tengchong Volcano-Geothermal Area, western Yunnan, China. Tectonophysics, 380: 69-87.

Wang, E.C., and Burchfiel, B.C., 2000. Late Cenozoic to Holocene deformation in southwestern Sichuan and adjacent Yunnan, China, and its role in formfation of the southeastern part of the Tibetan Plateau. Geol. Soc. Am. Bull., 112(3): 413-423.

Wang, J.H., Yin, A., Harrison, T.M., Grove, M., Zhang, Y.Q., and Xie, G.H., 2001. A tectonic model for Cenozoic igneous activities in the eastern Indo-Asian collision zone. Earth Plant. Sci. Lett., 188: 123-133.

Wang, J.Y., and Huang, S.P., 1988. Compilation of heat flow data in the China continental area. Sci. Geol. Sin., 2:196-204.

Wu, Q.F., Zu, J.H., and Xie, Y.Z., 1988. Basic geothermal characteristics in Yunnan Province (in Chinese). Seismol. Geol., 10(4): 177-183.

Xu, Y.G., Menzies, M.A., Thirlwall, M.F., and Xie, G.H., 2001. Exotic lithosphere mantle beneath the western Yangtze craton: Petrogenetic links to Tibet using highly magnesian ultrapotassic rocks. Geology, 29 (9): 863-866.

748 Yao, H.J., van der Hilst, R.D., and de Hoop, M.V., 2006. Surface-wave array
749 tomography in SE Tibet from ambient seismic noise and two-station analysis - I.
750 Phase velocity maps. Geophy. J. Int., 166: 732-744.
751 Yao, H.J., Beghein, C., van der Hilst, R.D., 2007. Surface-wave array tomography in
752 SE Tibet from ambient seismic noise and two-station analysis: II - Crustal and
753 upper mantle structure. Gephys. J. Int., submitted.
754 Yuan, X.H., Ni, J., Kind, R., Mechie, J., and Sandvol, E., 1997. Lithospheric and
755 upper mantle structure of southern Tibet from a seismological passive source
756 experiment. J. Geophy. Res., 102 (B12): 27491-27500.
757 Zhang, J., and Langston, C.A., 1995. Dipping structure under Dourbes, Belgium,
758 determined by receiver function modeling and inversion. Bull. Seis. Soc. Am., 85
759 (1): 254-268.
760 Zhu, L.P., Owens, T.J., and Randall, G.E., 1995. Lateral variation in crustal structure
761 of the northern Tibetan plateau inferred from teleseismic receiver functions. Bull.
762 Seis. Soc. Am., 85(6): 1531-1540.
763 Zhu, L.P., and Kanamori, H., 2000. Moho depth variation in southern California from
764 teleseismic receiver functions. J. Geophys. Res., 105 (B2): 2969-2980.
765 Zorin, Yu.A., Mordvinova, V.V., Turutanov, E.Kh, Belichenko, B.G., Artemyev, A.A,
766 Kosarev, G.L., and Gao, S.S, 2002. Low seismic velocity layers in the Earth's
767 crust beneath Eastern Siberia (Russia) and Central Mongolia: receiver function
768 data and their possible gological implication. Tectonophysics, 359: 307-327.
769
770

771

772 Figure captions

773 Figure 1. Location of seismic stations (red triangles) and cross-sections (blue lines) in
774 the study region (boxed area on the inset map). Red cross represents the Konga Shan
775 area. The background shows the topography of southeastern Tibet and the regional
776 faults: 1. Longmen Shan fault; 2. Xianshuihe fault; 3. Lijiang fault; 4. Zhongdian fault; 5.
777 Anninghe fault; 6. Xiaojiang fault; 7. Ailaoshan Red-River fault. The main geological
778 units are: SG, Songpan-Ganze fold system; YZ, Yangtze platform; SJ, Sangjiang fold
779 zone; SC, Sichuan basin [modified from Chen et al., 1987 and Wang et al., 2003]. The
780 Bomi-Tengchong fold system is located outside of the mapped area, starting ~ 80 km to
781 the west of station MC21.

782

783 Figure 2. A schematic representation of receiver functions: (a) simplified ray diagram
784 showing the main *P*-to-*S* converted phases for a layer over a half-space, and (b)
785 corresponding receiver function waveform. Vertical, radial, and transverse components
786 of the wavefield are denoted Z, R, and T, respectively. Except for the first arrival, upper
787 case letters denote downgoing travel paths, lower case letters denote upgoing travel paths,
788 and h indicates reflection from the interface [modified from Ammon et al., 1990].

789

790 Figure 3. Azimuthal projection centered on MC08 (black triangle) showing distribution
791 of events used in this study and recorded over the period September 2003 to October
792 2004. Small circles mark epicentral distance of 30º, 60º, and 90º from MC08. Two

793 red circles (A and B) indicate regions that saw frequent seismic activity during the
794 recording period (see also Figure 4).
795
796 Figure 4. Receiver functions calculated at stations MC22 (a-b) and MC05 (c-d). (a
797 and c) Waveform sections showing individual, radial receiver functions in the time range
798 spanning 5 s before to 40 s after the direct *P* arrival. The events are ordered by
799 increasing back azimuth, with back azimuths and epicentral distances for each event
800 shown in the right column. A and B denote clusters of events from Japan and the
801 Fiji-Tonga Islands, respectively (see Figure 3). (b and d) Radial (thick black line) and
802 transverse (thin blue line) receiver functions obtained by simultaneous deconvolution of
803 all high-quality traces recorded at each station (see Table 1). The traces are moveout
804 corrected for *P*-to-*S* conversions occurring between 0-500 km depth underneath the
805 stations, with a reference ray parameter of 0.0586 s/km corresponding to earthquakes at
806 ~67º epicentral distance, and they are filtered using a Gaussian filter with a width of 2.0
807 Hz.
808
809 Figure 5. Radial receiver functions from 25 temporary stations and station KMI
810 obtained by simultaneous deconvolution. *P*-to-*S* conversions from the Moho
811 discontinuities are indicated by downward red triangles.
812
813 Figure 6. Slant-stacking results for stations MC22 and MC05. (a and c) Receiver
814 functions ordered by ray parameter (*p*) for station MC22 and MC05, respectively, along
815 with predicted travel time curves estimated from the optimum solution of *H* and V_P/V_S,

determined by slant-stacking analysis (V_P = 6.2 km/s). These curves (dashed for arrivals that are more tentative) were generated using a simple, flat-Earth, and one-layer crust model. (b and d) Solution surfaces constructed by a direct search over V_P/V_S vs. H space. The optimum solution is indicated by a cross; contour lines are spaced at intervals of 0.1. Scale is normalized and all solutions with negative sum are shaded black.

Figure 7. Least-squares inversion and grid-search (i.e., simplified modeling) results for 8 stations. Results for each station are shown in two panels. The left panel shows the observed receiver function (thick black lines), its standard deviation (±σ) bounds (grey shading), and the synthetic receiver function corresponding to the grid-search solution (thin black line). The right panel shows the initial model (thin dashed lines), the preferred solution (thin black lines) from many-layered least-squares inversion, and the grid-search solution (thick black line). Results for all stations are presented in Figure A11.

Figure 8. Contour map of crustal thickness (in km) from this receiver function study. The orange line denotes the region of high Poisson's ratio (> 0.30). The red triangles represent stations with an obvious IC-LVZ, the blue ones represent stations without obvious IC-LVZ, and the black ones represent stations without sufficient data quality. The Sichuan basin is outlined by a thin blue line. Tectonic labels are the same as in Figure 1.

Figure 9. Comparison between crustal thicknesses obtained in this study, H_{RF}, and those from previous seismic refraction, H_{SR}, and gravity anomaly and deep seismic sounding profile data, H_{GRA} (Zhu et al., 2003, personal communication; Wang et al., 2003). Correlation coefficients are 0.88 between H_{RF}-H_{SR}, and 0.86 between H_{RF}-H_{GRA}.

Figure 10. Elevation and velocity cross-sections along Line 1 in Figure 1. Top: Topography profile and (projected) locations of the stations (red triangles) and major fault zones. Bottom: *S*-wave velocity models (IC-LVZ = Intracrustal low-velocity zone). The Moho depth (inferred from slant-stacking analysis) is indicated by black arrows.

Figure 11. Same as Figure 10 but for Line 2 in Figure 1.

Structure of the crust beneath the Southeastern Tibetan Plateau from Teleseismic Receiver Functions - Appendices

Lili Xu, Stéphane Rondenay, Robert D. van der Hilst

Appendix I – Least-squares inversion of receiver function waveforms: strategy and robustness of the observations

The least-squares inversion applied in this study is a modified version of the method proposed by Ammon et al. (1990). The strategy adopted here consists of two stages: first, a "many-layered inversion" in which the crust is parameterized through a large number of layers which produce a very good fit to the data but result in a overly smooth

model and, second, a "simplified forward modeling" in which the crust parameterization is reduced to the minimum number of layers necessary to fit the data within a prescribed confidence interval. Here, we describe the misfit criterion chosen at both stages to insure that resulting models are robust in a statistical sense, and we address issues such as the dependence of the resulting model on the starting model, the transition from many-layered to simplified parameterization, and the robustness of mid-crustal structure.

1) Multi-layered inversion

A well-documented problem in the inversion of receiver function waveforms is the dependence of the resulting model on the starting model (see, e.g., Ammon et al., 1990). To address this issue in the many-layered inversion, the preferred resulting model is selected on the basis of a chi-squared misfit criterion applied to models derived from a range of starting models. A distribution of starting models is built by adding a composite of a cubic perturbation and a random perturbation to the layer velocities of the initial background model (see Ammon et al., 1990). Here, we create a distribution of 64 starting models by applying cubic perturbations with maximum amplitude between 0.5-1.0 km/s and random perturbations with variances between 0.1-0.2 km/s. We run an inversion for each of these starting models and produce a corresponding distribution of 64 resulting models. The preferred solution corresponds to the average of a family of models that fit the receiver function waveform within data uncertainty using a chi-squared test with 95% confidence (see Lodge and Helffrich, 2006). Examples of many-layered inversion results are shown for stations MC02 and MC05 in Figures A1

and A2, respectively. This approach allows us to introduce a robust misfit criterion and to take into account the dependence of the solution on the starting model.

Since the distribution of starting models does now produce a large range of velocities in the underlying half-space (see Figures A1-A2), we conduct further testing to assess the robustness of intra-crustal structure recovered by inversion as a function of the half-space velocity in the starting model. We run a set of many-layered inversion for MC05 in which the initial crustal velocities are as in Figure A2, but where the initial velocity in the upper mantle is varied (Figure A3). We note that the main effect of altering the half-space velocity is to modify the velocity gradient associated with the Moho (larger gradients result from larger velocity contrasts at the base of the initial models), but that in all cases the intra-crustal structure – in particular the IC-LVZ – is preserved and required by the data.

2) Simplified forward modeling

As shown in Figures A1-A2, the many-layered inversion tends to overfit the data and introduces too much structure in the solution. To guard against this, we use the preferred solution of the many-layered inversion as a basis to construct simple 2-5 layer models that can still fit the receiver function waveform within data uncertainty using a chi-squared test with 95% confidence (see Lodge and Helffrich, 2006). For each station, we identify the necessary structure by investigating the effects of isolated portions of the many-layered solutions on the receiver function waveform and replacing these structural elements with single sharp discontinuities (see examples for station MC02-MC05 in

Figures A4-A10). After determining the minimum amount of structure needed, we perform a grid search over the parameters of the simplified model (layer velocities and Moho depth) and perform the chi-squared test to identify the ensemble of solutions that fit the data within 95% confidence (Lodge and Helffrich, 2006). The preferred simplified model corresponds to the mean of this ensemble of acceptable solutions. This approach produces models that are more realistic and, therefore, easier to interpret.

In cases where the many-layered inversion returns a solution containing an IC-LVZ, we proceed with the analysis described above by constructing a simple 2-5 layer model with and without a low-velocity zone at mid-crustal depth and verify that the IC-LVZ is necessary to fit major elements of the receiver function waveform. In the example for station MC05 shown in Figures A7-A10, we note that a large-amplitude trough in the receiver function signal at ~2 and 6 s does require the presence of a low-velocity layer bounded by sharp boundaries at ~15 and ~38 km depth. Therefore, robust IC-LVZs are assigned only in cases where both the many-layered inversion solution and the simplified forward modeling require the presence of low-velocities in the crust to explain parts of the receiver function waveform.

Appendix II – Inversion results

Figure A11 shows the preferred models from many-layered inversion and simplified forward modeling of receiver function waveforms recorded at all the seismic stations investigated in this study (categories 1-2 in Table 1).

930

931 **Appendix III – Crustal Poisson's ratio: What does slant-stacking tell us?**

932

933 The slant-stacking approach of Zhu and Kanamori (2000) described in section 2.2 of the
934 paper returns a single, average estimate of the Poisson's ratio for the whole crustal
935 column. To formulate a meaningful interpretation of such estimate in the context of a
936 thick, possibly channeled crust as that which is inferred in the SE Tibetan plateau, we
937 must investigate the effects of layered crustal structure on the slant-stacking results. We
938 do this by conducting a series of synthetic tests with low-viscosity channels embedded in
939 otherwise "normal" crust. Although these are fairly simplified models that do not take
940 into account the effects of high Poisson's ratio due to mafic/ultramafic lower crust, they
941 do nevertheless provide a good sense of how the overall Poisson's ratio responds to
942 localized perturbations associated with weaker intra-crustal layers.

943 Synthetic waveforms of the *P*-coda are generated for a set of 3-layer crustal velocity
944 models (Table A1). The velocity models have an IC-LVZ with Poisson's ratio ranging
945 between 0.25-0.35 and a thickness range of 10-40 km, starting at 8 km depth. The
946 Poisson's ratio is normal (i.e., 0.25) outside this layer. Crustal thickness is kept constant
947 at 60 km. The corresponding synthetic receiver functions are produced by deconvolving
948 the vertical component from the radial component as with the field data. We then use
949 the slant-stacking technique of Zhu and Kanamori to derive Moho thickness (H) and
950 V_P/V_S ratio from these synthetic receiver functions. The results are presented in Figure
951 A12 and show that, as expected, the overall crustal Poisson's ratio derived from the
952 slant-stacking technique increases with the thickness and the Poisson's ratio of the

IC-LVZ. The overall crustal Poisson's ratio is averaged out over the entire crust and is thus always smaller than the Poisson's ratio in the LVZ. For example, a 10-km LVZ with Poisson's ratio of 0.35 will produce an overall crustal Poisson's ratio of 0.275.

Figure captions

Figure A1. Many-layered, least-squares inversion for station MC02. The left panel shows the observed, stacked receiver function (black solid line) and its standard deviation (grey shading). The red line denotes the synthetic receiver function from the preferred solution to the inverse problem. The right panel shows the range of starting models (outlined by black dashed line), the solutions that fit the data within 95% confidence (solid black lines), and the preferred solution (solid red line).

Figure A2. Same as Figure A1 but for station MC05.

Figure A3. Effects of the half-space S-velocity in the initial model on the least-squares solution. The least-squares inversion is performed for station MC05 with the same initial model in the crust as that used in Figure A2, but with upper mantle velocities of (a) 4.3 km/s, (b) 4.5 km/s, and (c) 4.8 km/s. Each case is presented in three panels: the upper left panel shows the observed receiver function (thick black line), its standard deviation (thin black lines), and the synthetic receiver function corresponding to the starting model (blue line); the lower left panel shows the observed receiver function (thick black line), its standard deviation (thin black lines), and the synthetic receiver

function corresponding to the least-squares solution (red line); the right panel shows starting velocity model (blue line), the least-squares solution that fits the data with 95% confidence (gray shading), and the preferred least-squares solution (red line).

Figure A4. Contributions from the many-layered inversion solution to the receiver function waveform recorded at station MC02 (Figure A1). Left panels show the observed receiver function (thick black line) and the synthetic receiver functions (thin grey lines) corresponding to components of the velocity model shown in the right panel. For each component, the velocity at the base of the dashed-line box is extrapolated into a half-space forming the base of the model. Component (a) comprises a surface low-velocity layer that produces a time shift of the incident P-arrival by and multiples in the 0-5 s time interval. Component (b) comprises a positive gradient between ~35-50 km depth that produces a positive *P*-to-*S* pulse at ~5.9 s.

Figure A5. Construction of a simplified velocity model for station MC02 based on the on the many-layered inversion solution (Figures A1, A4). Definition of the panels as in Figure A4. Two successive velocity jumps in the top 10 km (a-b) are required to produce the time shift of the incident *P*-wave, and the first positive and negative pulses following P. A velocity jump at ~48 km depth (c) then is required to produce the large positive pulse at 5.9 s and later multiples.

Figure A6. Grid search over the parameters controlling the simplified model constructed for station MC02 (Figure A5). Left panel shows the observed receiver function (thick

black line) and the synthetic receiver function corresponding to the preferred solution (red line). Right panel shows the range (black dashed lines) over which the grid search is performed for the following parameters: V_S, V_P/V_S, and the Moho depth. Density is calculated using the equation $\rho = 0.32\ V_P + 0.77$ (Berteussen, 1977). The thin black lines indicate the models that fit the data within 95% confidence, and the red line indicates the preferred solution.

Figure A7. Contributions from the many-layered inversion solution to the receiver function waveform recorded at station MC05 (Figure A2). Definition of the panels and model components as in Figure A4. Component (a) comprises a surface low-velocity layer that produces a time shift of the incident P-arrival by and multiples in the 0–5 s time interval. Component (b) comprises a negative gradient centered on ~10 km depth that causes a negative pulse at ~2 s and further multiples in the 2–10 s time interval. Component (c) comprises a positive velocity gradient between ~50-65 km depth that produces a positive *P*-to-*S* pulse at ~7.3 s.

Figure A8. Construction of a simplified velocity model for station MC05 based on the many-layered inversion solution (Figures A7), without an IC-LVZ. Definition of the panels as in Figure A5. A velocity jumps at ~2 km depth (a) is required to produce the time shift of the incident *P*-wave. A second velocity jump at ~38 km depth (c) is required to produce the pulse at 4.9s. A third, larger velocity jump at ~56 km depth (d) is required to produce the large positive pulse at 5.9 s and later multiples. Note that

parts of the receiver function signal in the 0–10 s time range are not well fitted, in particular troughs at ~2 and 6 s.

Figure A9. Construction of a simplified velocity model for station MC05 based on the many-layered inversion solution (Figures A7), with an IC-LVZ. Definition of the panels as in Figure A5. A negative gradient (b) added to the simplified model in Figure A8 produces the troughs necessary to fit the receiver function waveform at ~2 and 6 s.

Figure A10. Grid search over the parameters controlling the simplified model constructed for station MC05 (Figure A9). Definition of the panels as in Figure A6.

Figure A11. Least-squares inversion and grid-search (i.e., simplified modeling) results for stations MC01-MC25. Results for each station are shown in two panels. The left panel shows the observed receiver function (thick black lines), its standard deviation ($\pm\sigma$) bounds (grey shading), and the synthetic receiver function corresponding to the grid-search solution (thin black line). The right panel shows the initial model (thin dashed lines), the preferred solution (thin black lines) from many-layered least-squares inversion, and the grid-search solution (thick black line).

Figure A12. Effect of an intracrustal layer with variable thickness and Poisson's ratio on the average crustal Poisson's ratio calculated by the method of Zhu and Kanamori (2000). Straight lines represent four possible layer thicknesses (10-40 km) and show for each

case the average crustal Poisson's ratio (ordinate) as function of the layer's Poisson's ratio (abscissa). The velocity model used to calculate this graph is shown in Table A1.

Table 1. Station information and receiver function results.

Station	latitude (°N)	longitude (°E)	Number of traces	Moho depth #1 (km) [2]	V_P/V_S ratio [2]	Poisson's ratio [2]	Moho depth #2 [3]	Moho depth #3 [4]	Category [5]
MC01	31.0	102.3	70	64.0 ± 1.0	1.66 ± 0.03	0.21 ± 0.01	58.6	54	2
MC02	30.4	103.4	51	46.0 ± 1.0	1.76 ± 0.08	0.26 ± 0.03	54.2	47	1
MC03	30.0	102.5	65	62.0 ± 2.0	1.96 ± 0.05	0.32 ± 0.01	56.6	52	2
MC04	30.1	101.5	57	58.0 ± 1.0	1.90 ± 0.06	0.31 ± 0.02	61	58	2
MC05	30.0	100.2	88 (42) [1]	59.0 ± 1.0	1.76 + 0.03	0.26 ± 0.01	62.5	60	2
MC06	28.9	99.8	57 (24) [1]	64.0 ± 1.0	1.74 ± 0.03	0.25 ± 0.01	61.5	58	2
MC07	29.0	100.4	65	58.5 ± 3.5	1.76 ± 0.15	0.25 ± 0.06	61.5	58.5	2
MC08	29.0	101.5	57	52.0 ± 1.0	1.92 ± 0.05	0.31 ± 0.01	56.9	56	2
MC09	29.0	102.8	32	49.0 ± 1.0	1.93 ± 0.08	0.31 ± 0.02	51.3	50	2
MC10	29.0	103.9	54	40.5 ± 1.5	1.84 ± 0.10	0.29 ± 0.03	48.7	44	2
MC11	28.3	103.1	78 (30) [1]	44.0 ± 1.0	1.95 ± 0.07	0.32 ± 0.02	48.2	47	2
MC12	27.7	102.2	29	-	-	-	56.7	49	3
MC13	27.7	100.8	87	57.0 ± 2.0	1.80 ± 0.05	0.27 ± 0.02	58.5	53	2
MC14	27.9	99.7	69	58.0 ± 2.0	1.73 ± 0.07	0.25 ± 0.03	58.6	54	2
MC15	26.8	100.0	52	47.0 ± 2.0	1.87 ± 0.08	0.30 ± 0.02	55.1	49	2
MC16	27.2	103.6	24	48.5 ± 1.5	1.66 ± 0.07	0.21 ± 0.04	50.9	45	2
MC17	26.5	101.7	39	48.5 ± 0.5	1.79 ± 0.06	0.27 ± 0.02	53	45.5	2
MC18	26.1	103.2	24	-	-	-	52.6	44.5	3
MC19	25.7	101.9	30	-	-	-	53	43.5	3
MC20	25.8	100.6	35	45.5 ± 1.5	1.79 ± 0.08	0.27 ± 0.03	48.1	45	2
MC21	25.5	99.6	51	46.0 ± 1.0	1.70 ± 0.06	0.23 ± 0.03	41.3	45	2
MC22	24.5	100.2	29	37.5 ± 1.5	1.74 ± 0.10	0.25 ± 0.04	41.3	43	1
MC23	24.9	101.5	62	48.0 ± 1.0	1.77 ± 0.07	0.26 ± 0.03	50.9	43	2
MC24	24.2	102.8	62	37.0 ± 5.0	1.90 ± 0.18	0.30 ± 0.05	41.6	41.5	1
MC25	24.9	103.7	59	43.5 ± 1.5	1.68 ± 0.10	0.22 ± 0.05	44.6	42	2
KMI	25.1	102.7	70	-	-	-	48.4	43	3

1. Total number of traces (events) used for receiver function analysis at each station
2. Moho depth, V_P/V_S ratio, and Poisson's ratio from this receiver function study
3. Moho depth from seismic refraction profiles (Zhu et al., personal communication, 2003)
4. Moho depth gravity anomaly/deep seismic sounding profile results (Wang et al., 2003)
5. Measures the reliability of the crustal properties derived from slant-stacking analysis; 1 is highest and 3 is lowest, see text for details

Table A1. Velocity model for Poisson's ratio test

Layer number	Thickness (km)	V_P (km/s)	V_S (km/s)	Density (g/cm^3)	Poisson's ratio
1	8	6.06	3.50	2.71	0.25
2	10-40	6.00	2.88-3.46	2.69	0.25-0.35
3	42-12	6.54	3.78	2.86	0.25
4	∞	8.00	4.62	3.33	0.25

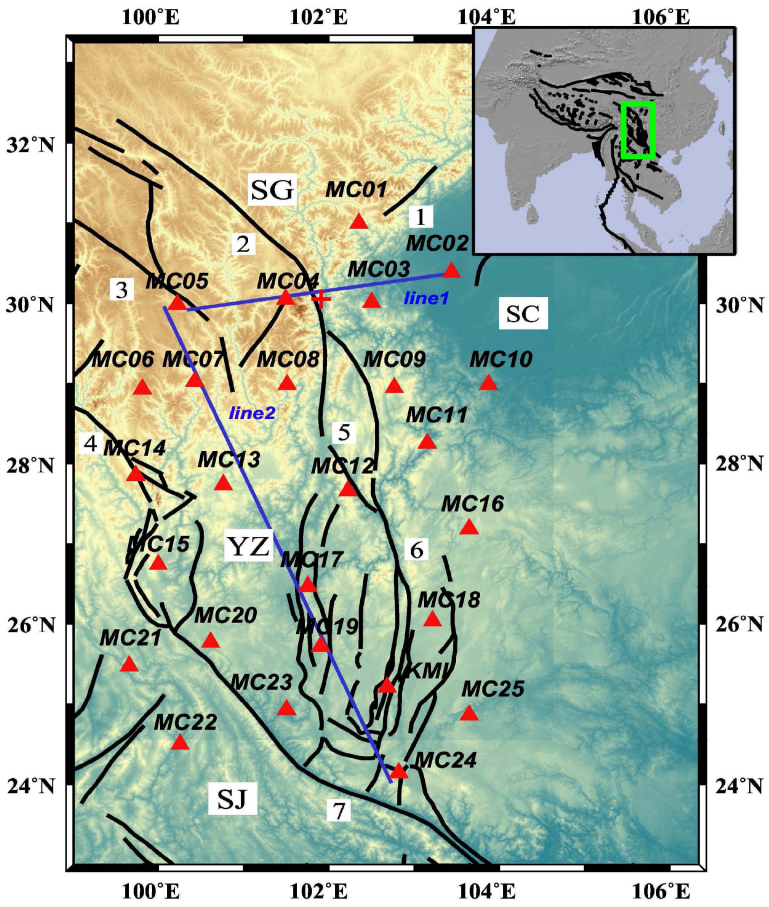

Figure 1
Xu et al., 2007

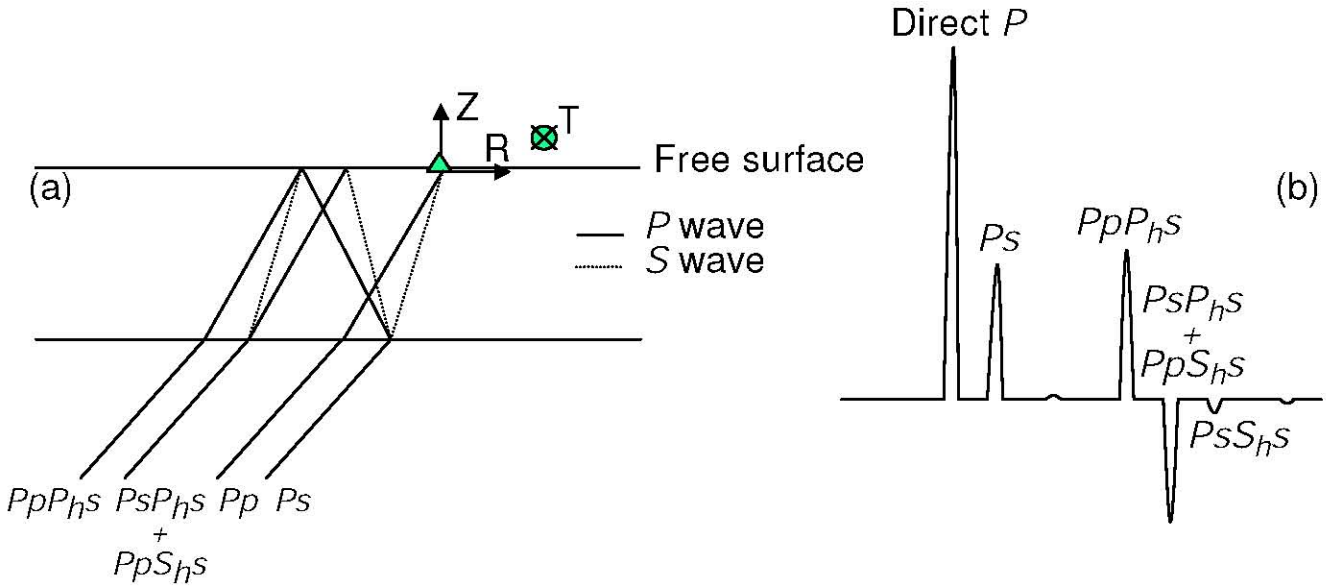

Figure 2
Xu et al., 2007

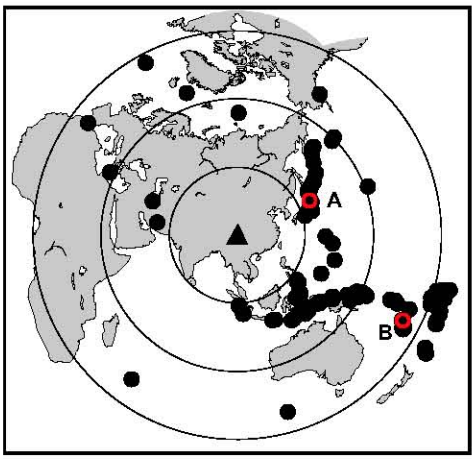

Figure 3
Xu et al., 2007

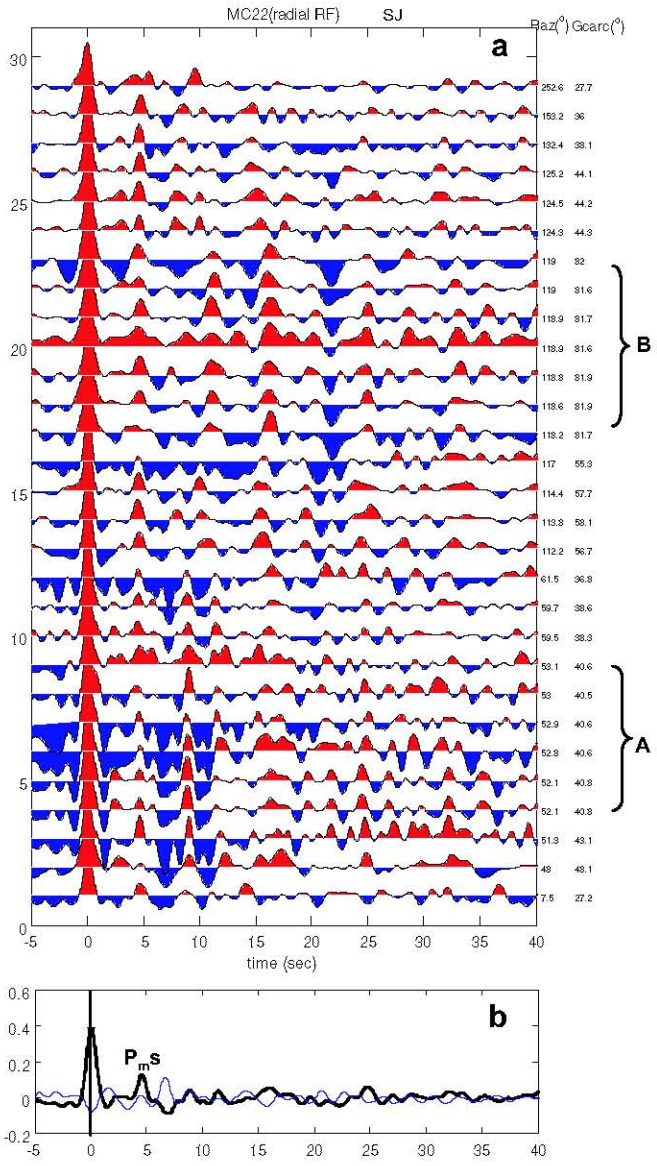

Figure 4
Xu et al., 2007

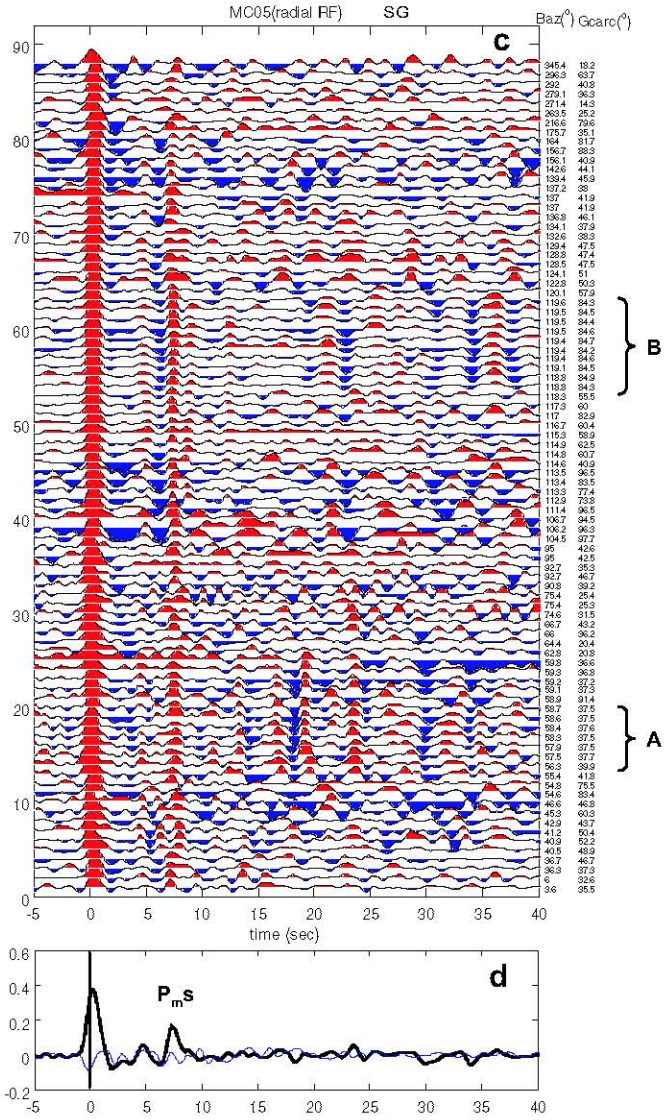

Figure 4 (continued)
Xu et al., 2007

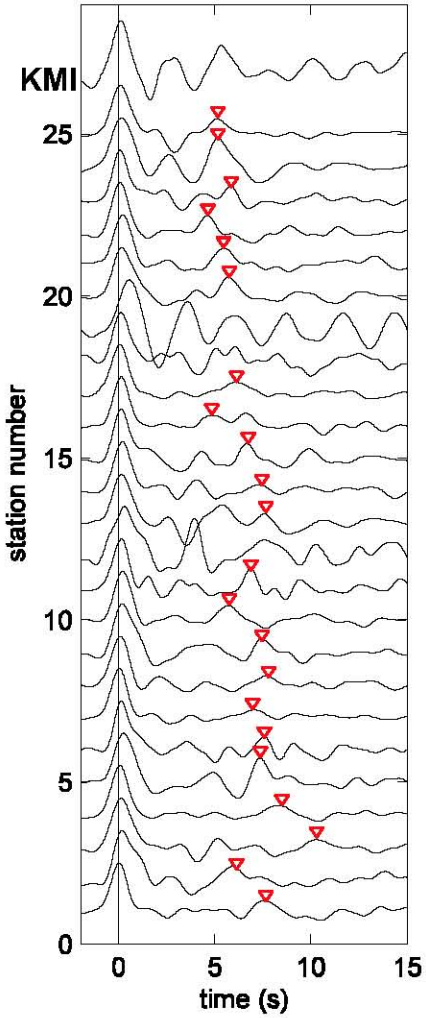

Figure 5
Xu et al., 2007

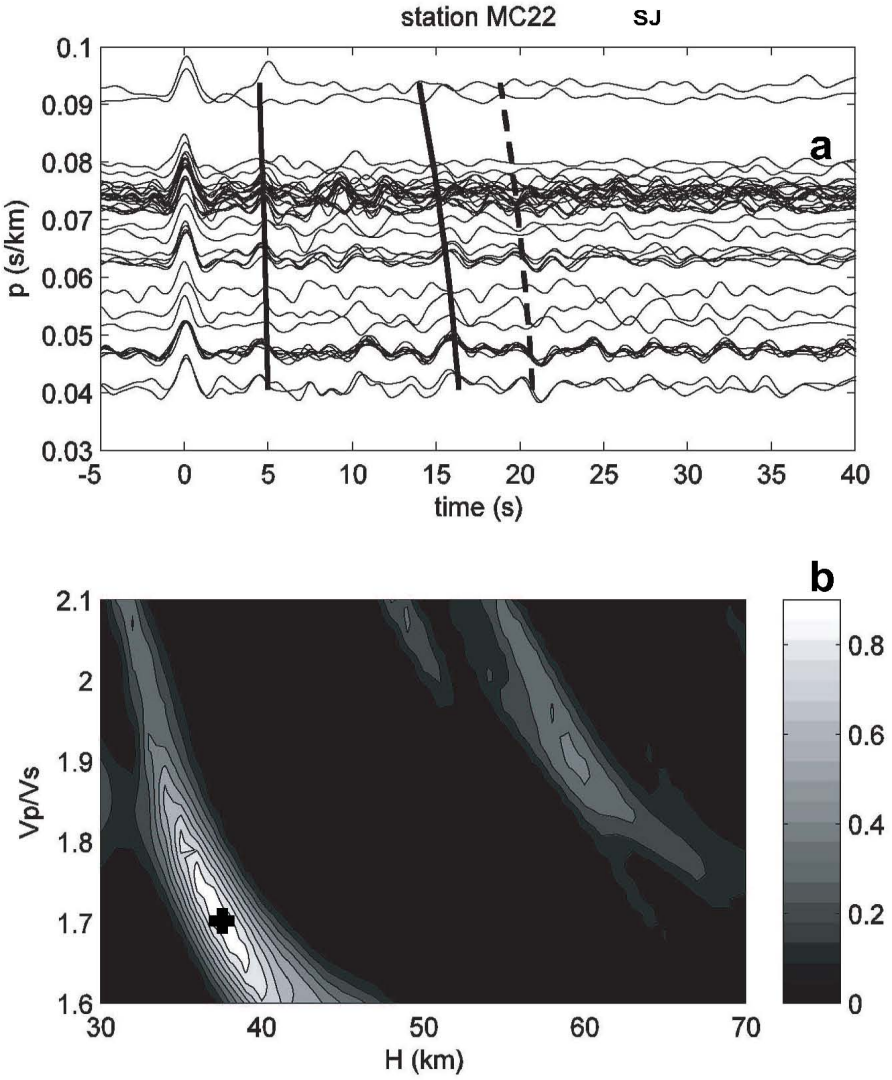

Figure 6
Xu et al., 2007

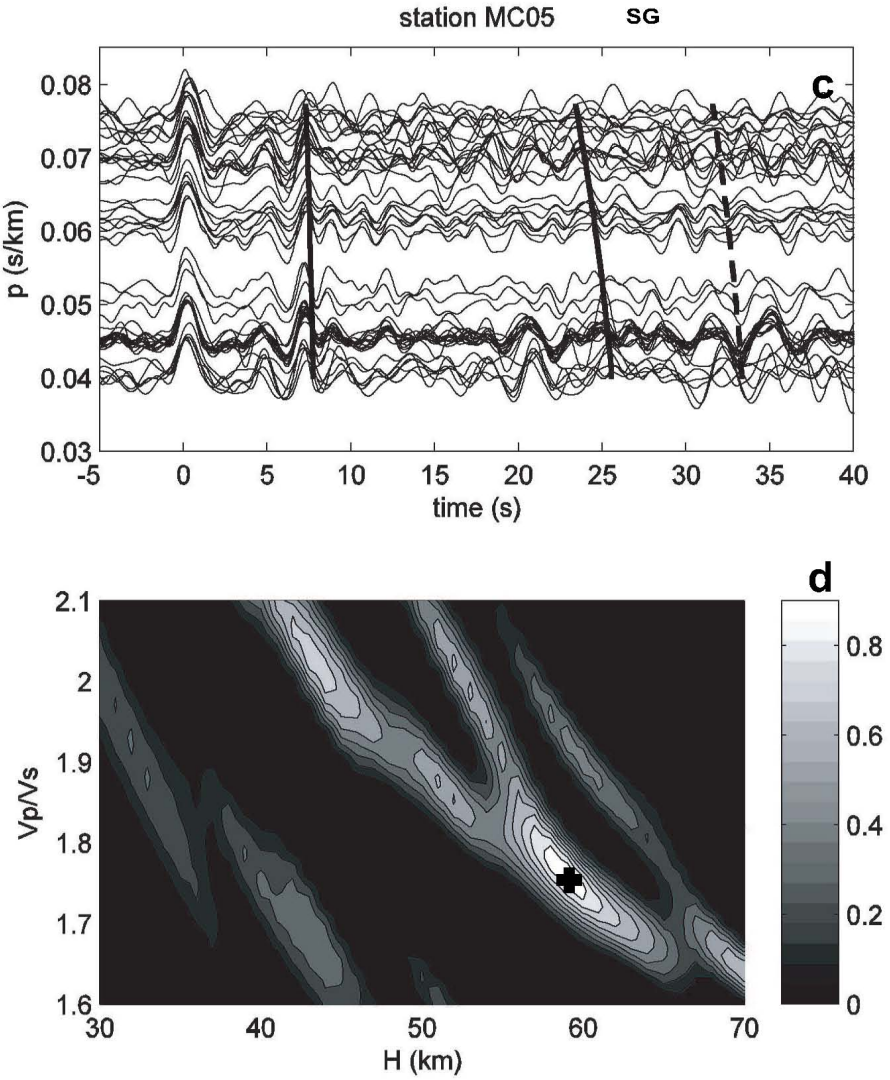

Figure 6 (continued)
Xu et al., 2007

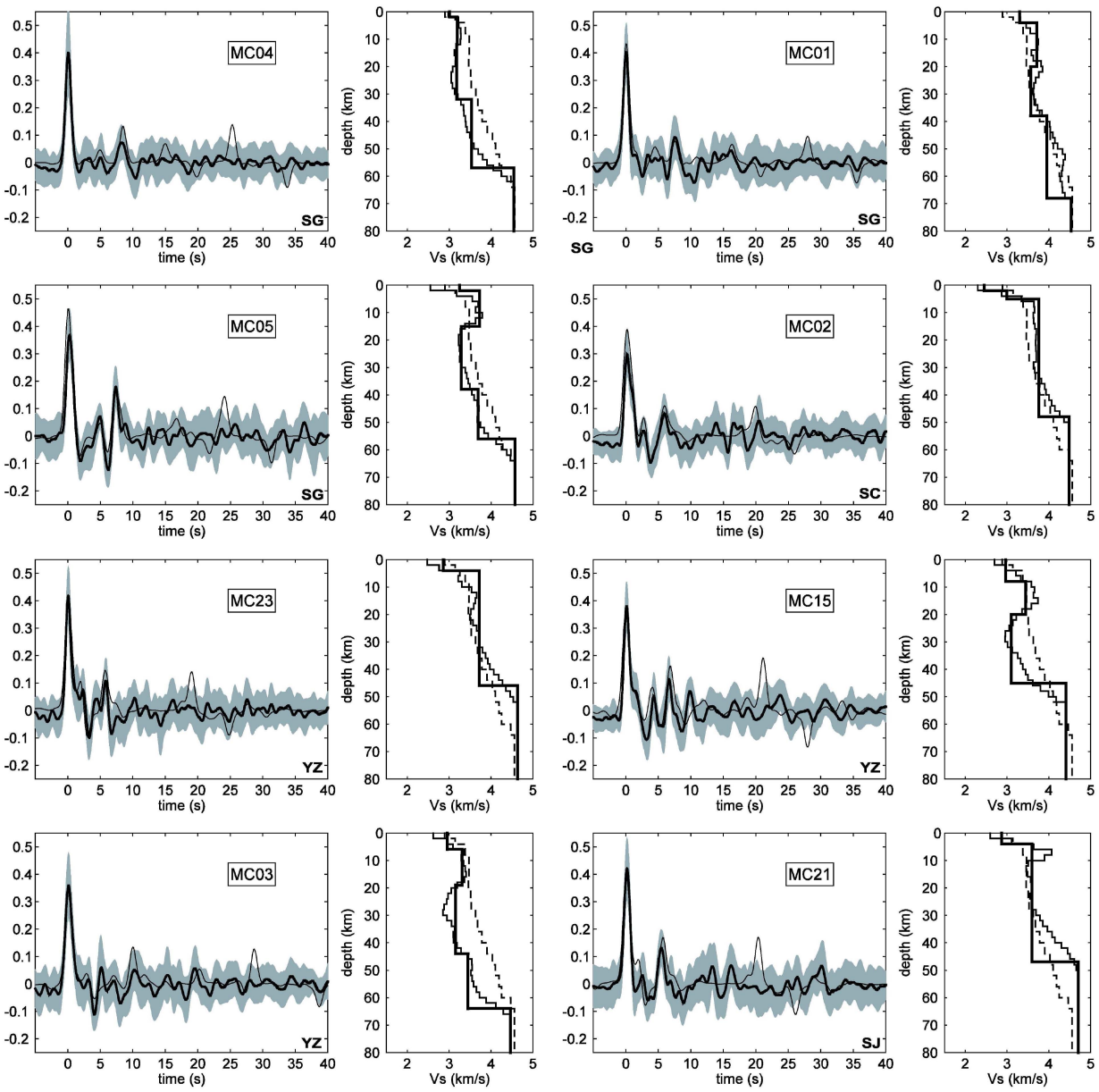

Figure 7
Xu et al., 2007

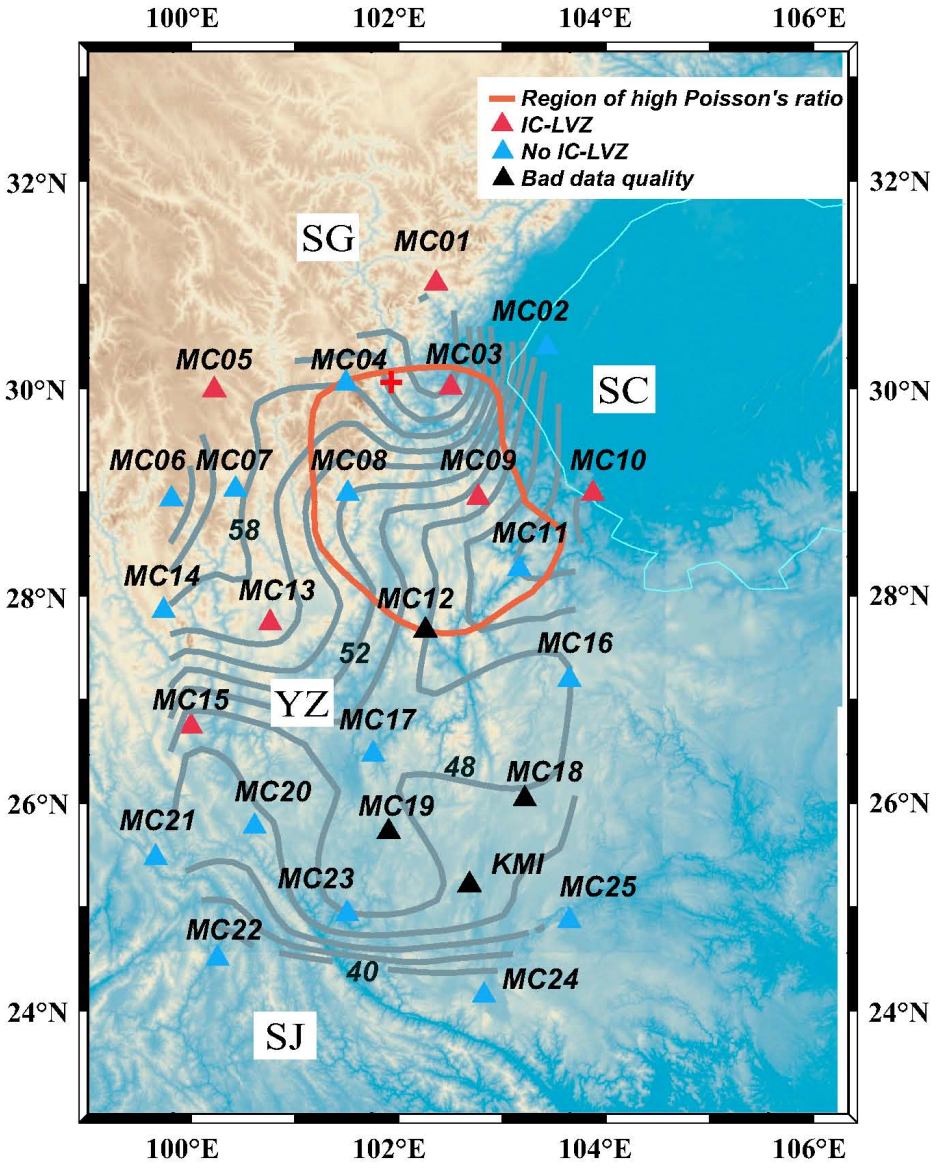

Figure 8
Xu et al., 2007

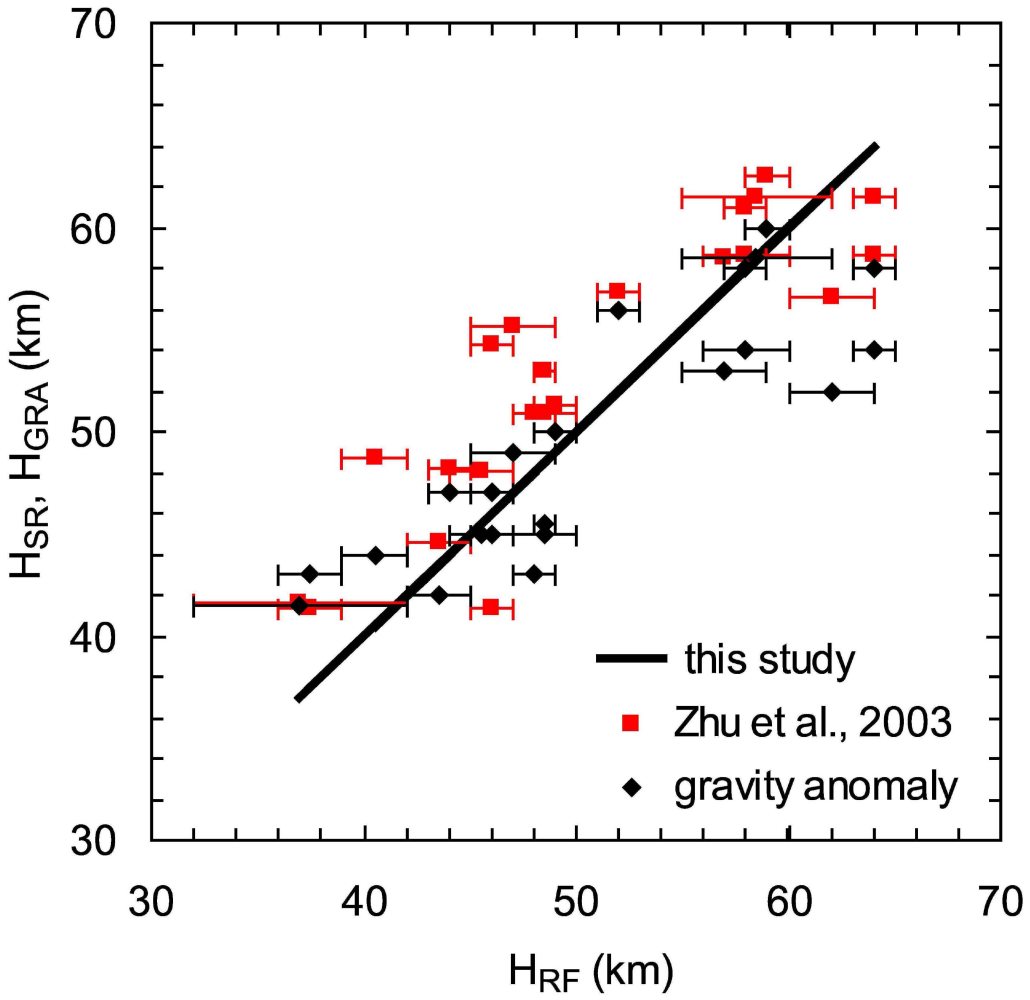

Figure 9
Xu et al., 2007

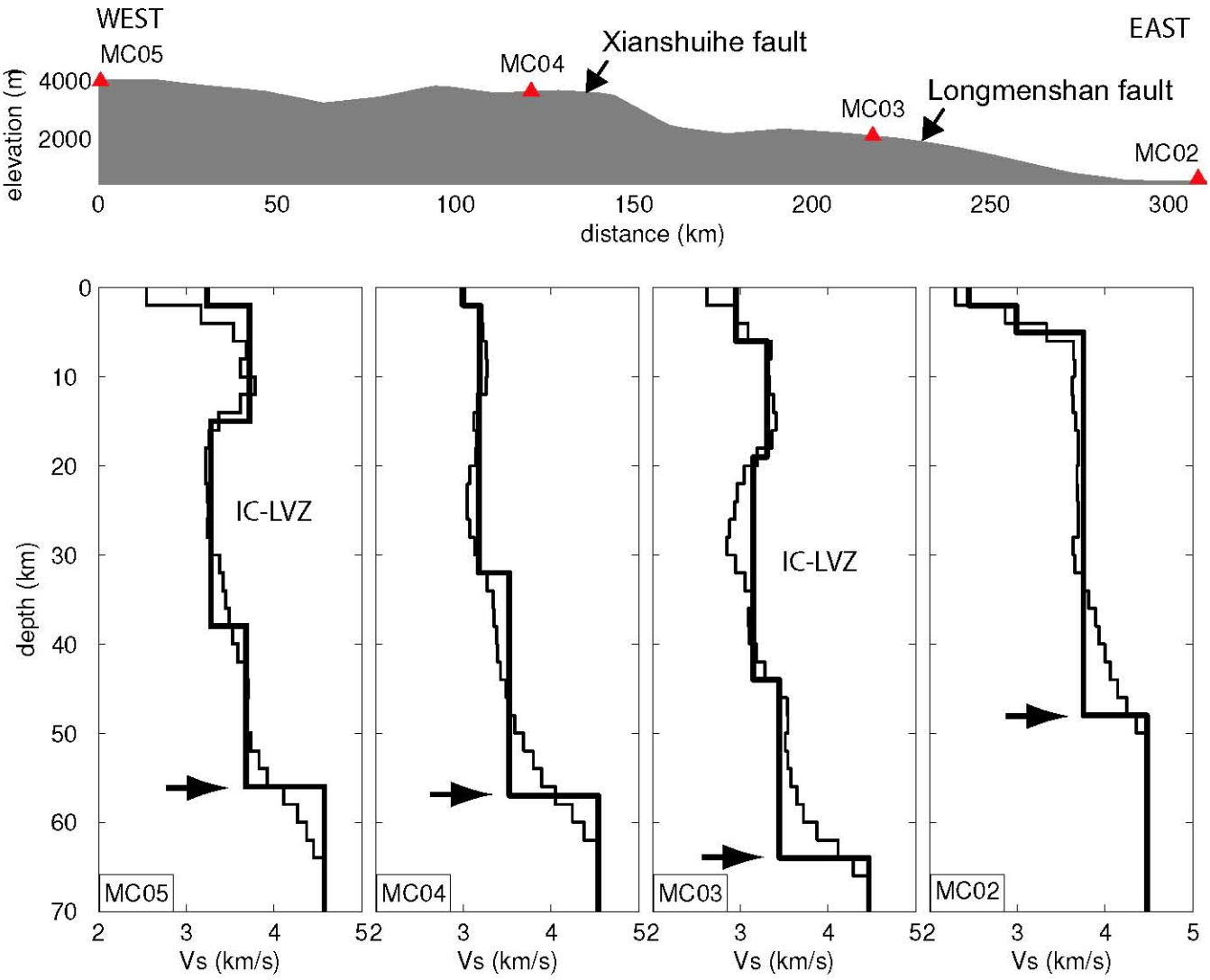

Figure 10
Xu et al., 2007

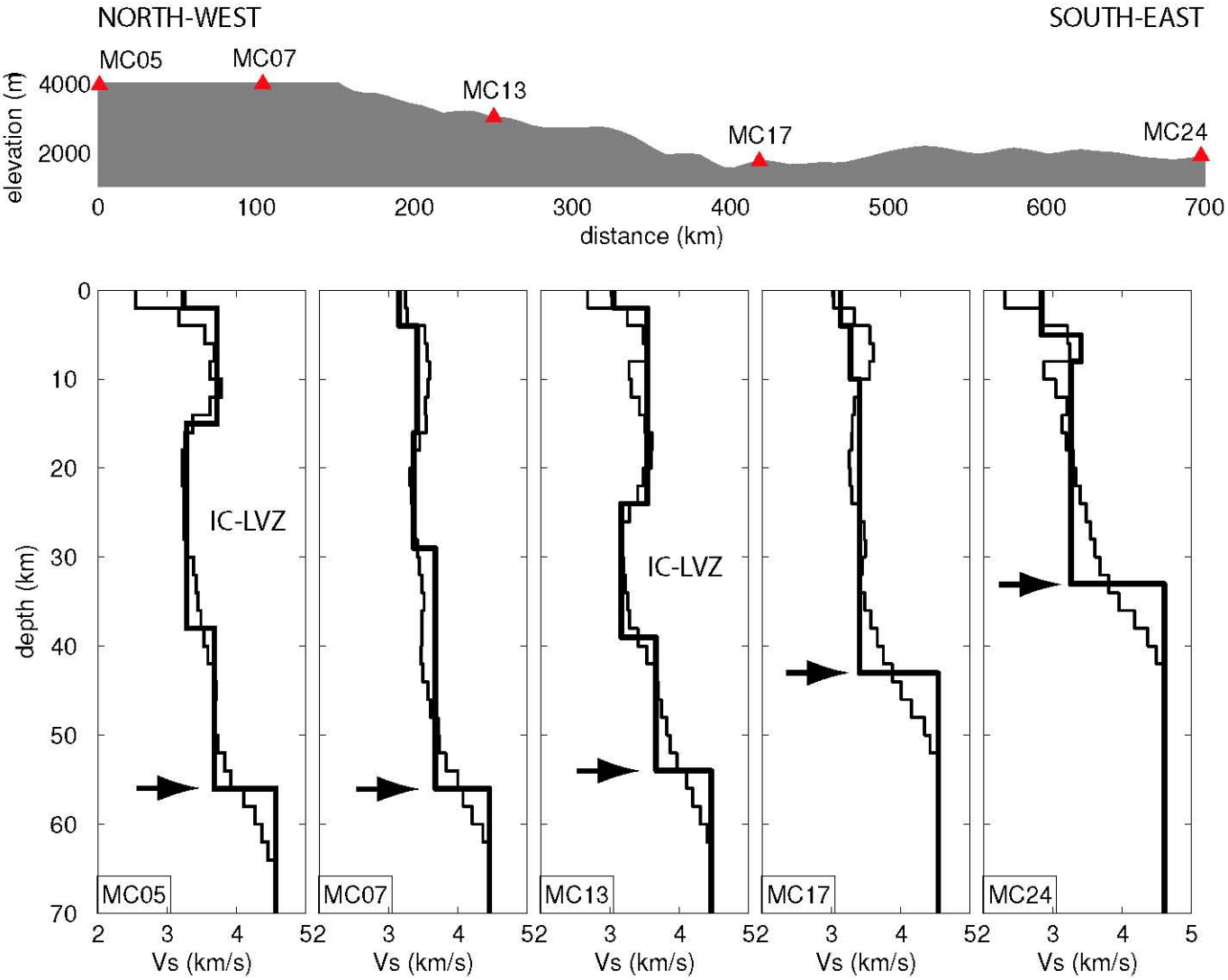

Figure 11
Xu et al., 2007

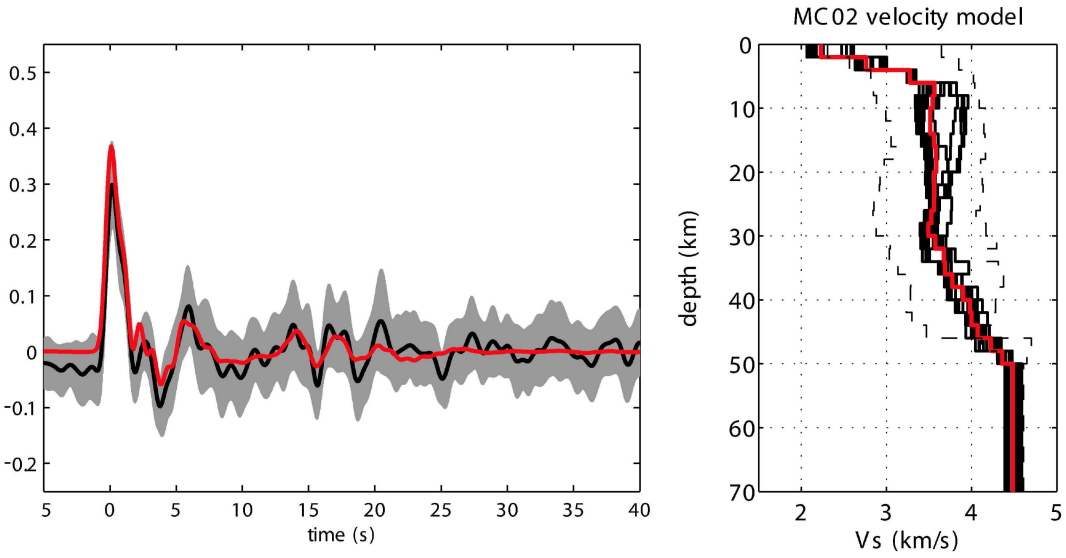

Figure A1
Xu et al., 2007

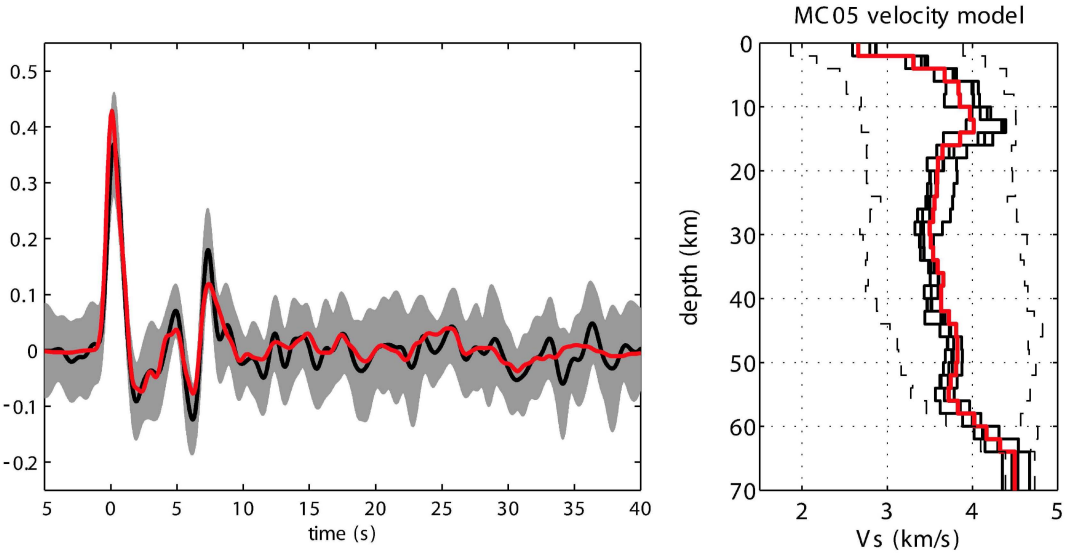

Figure A2
Xu et al., 2007

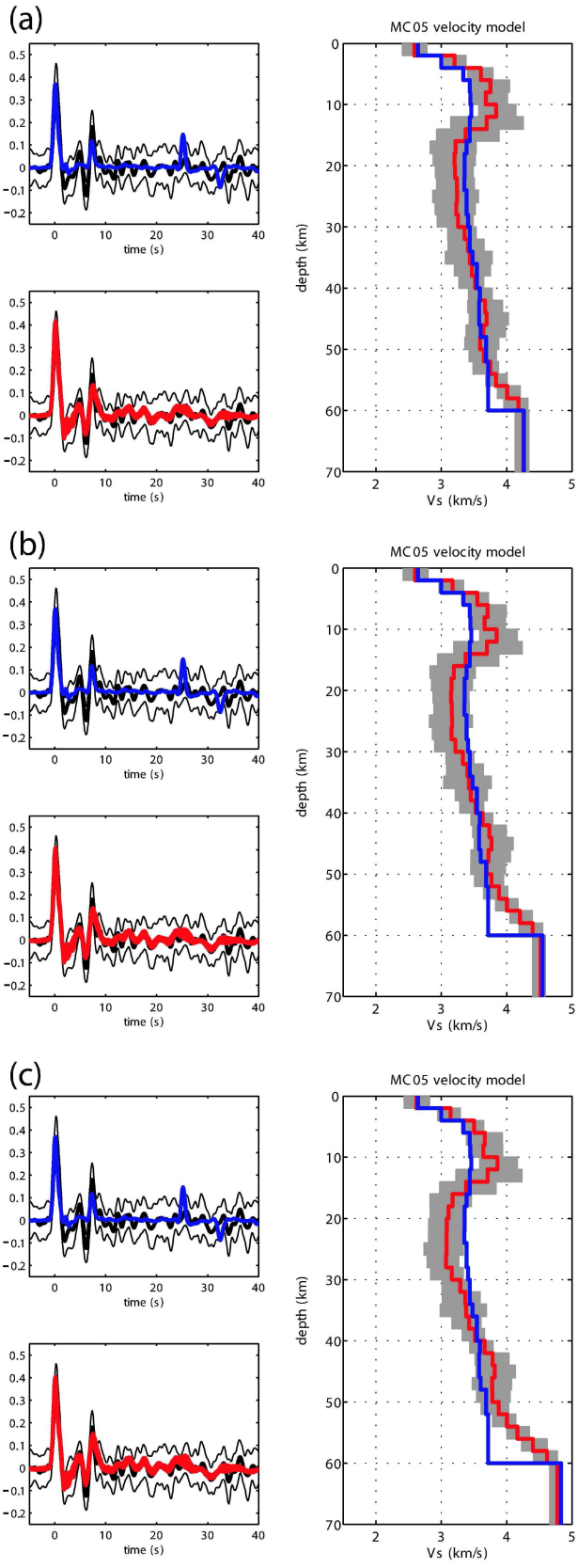

Figure A3
Xu et al., 2007

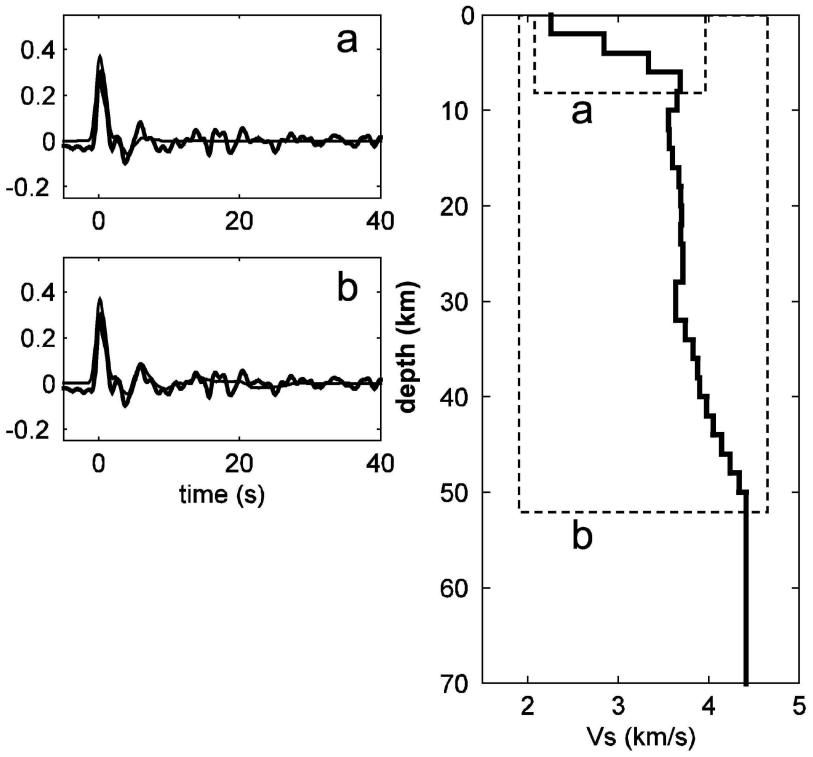

Figure A4
Xu et al., 2007

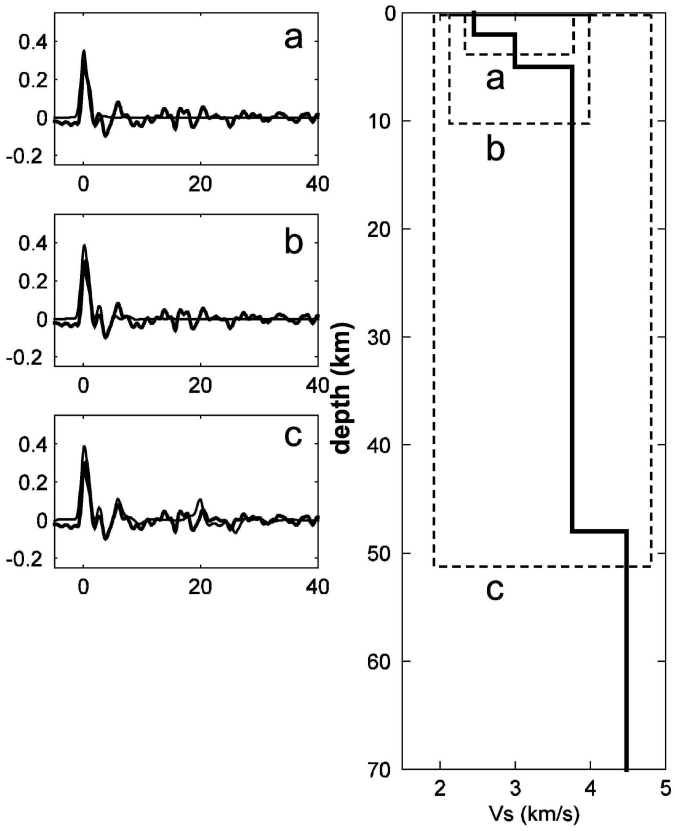

Figure A5
Xu et al., 2007

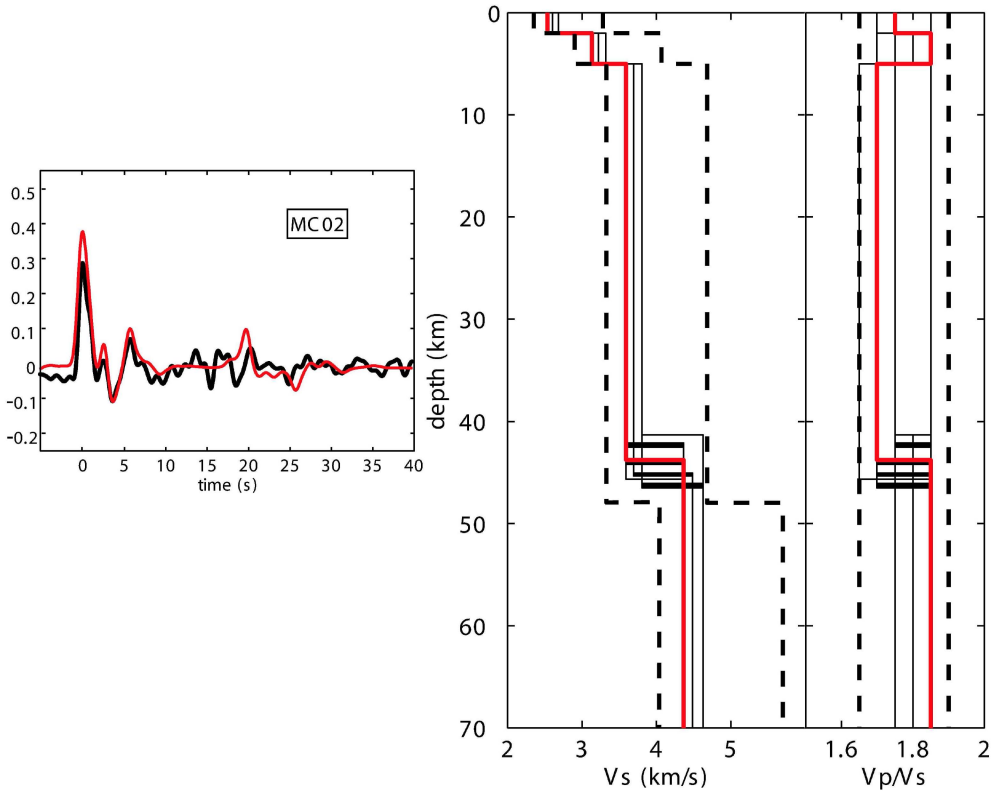

Figure A6
Xu et al., 2007

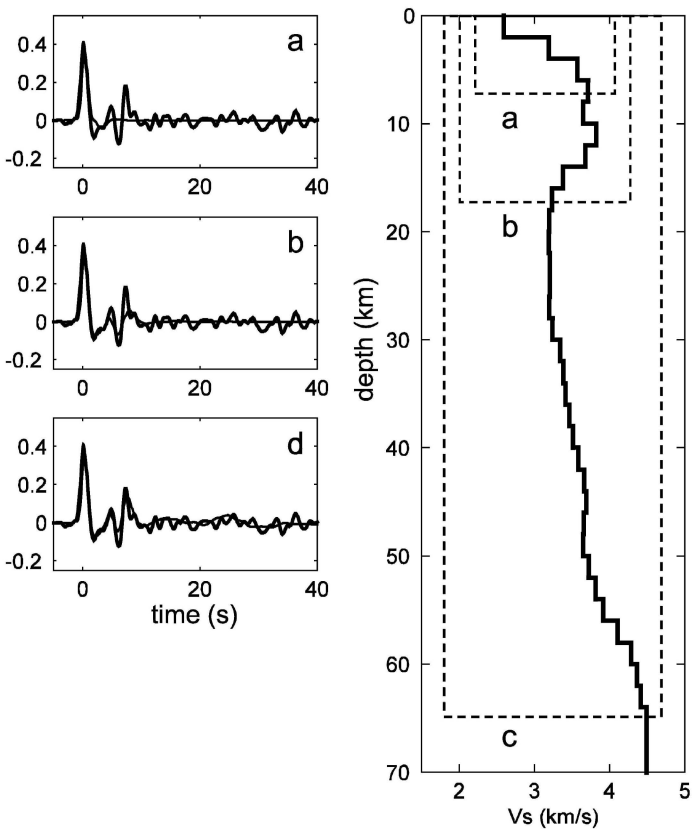

Figure A7
Xu et al., 2007

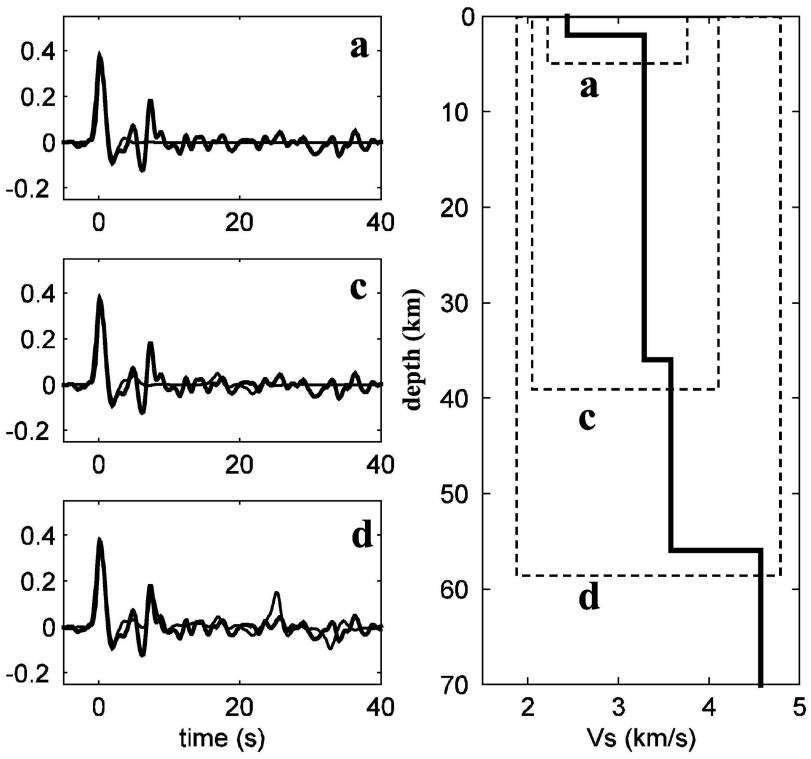

Figure A8
Xu et al., 2007

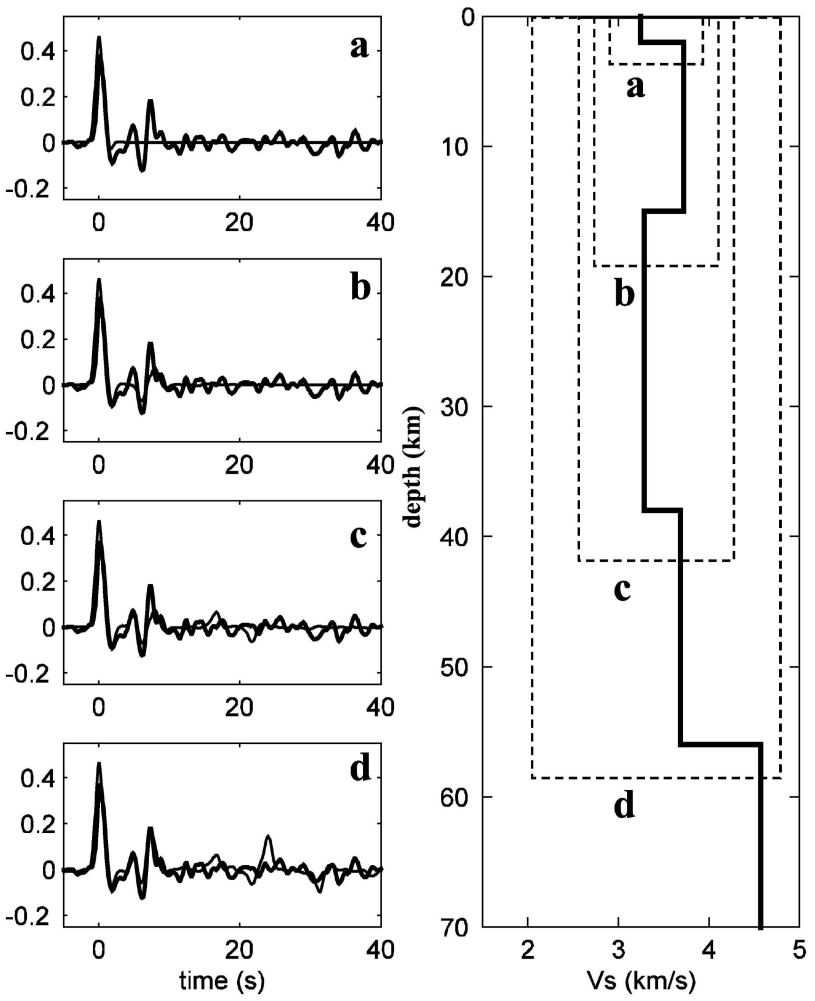

Figure A9
Xu et al., 2007

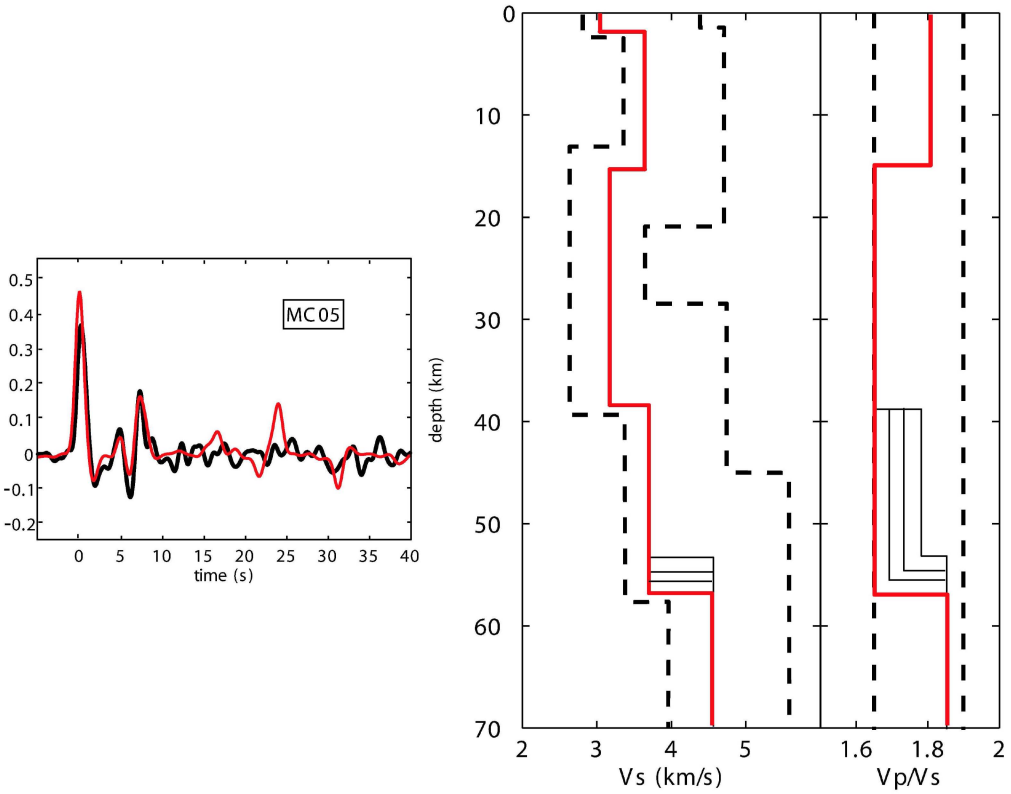

Figure A10
Xu et al., 2007

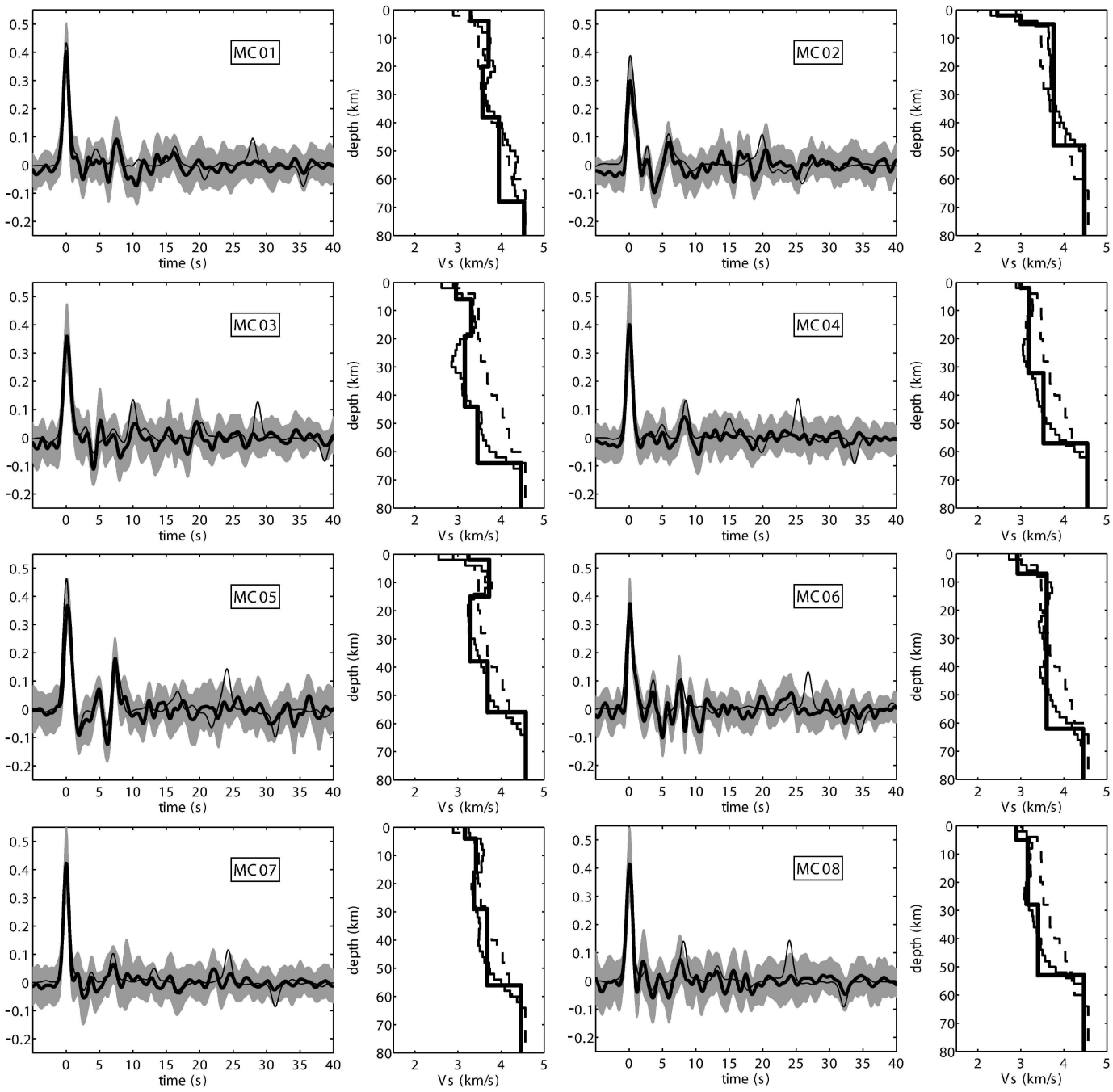

Figure A11
Xu et al., 2007

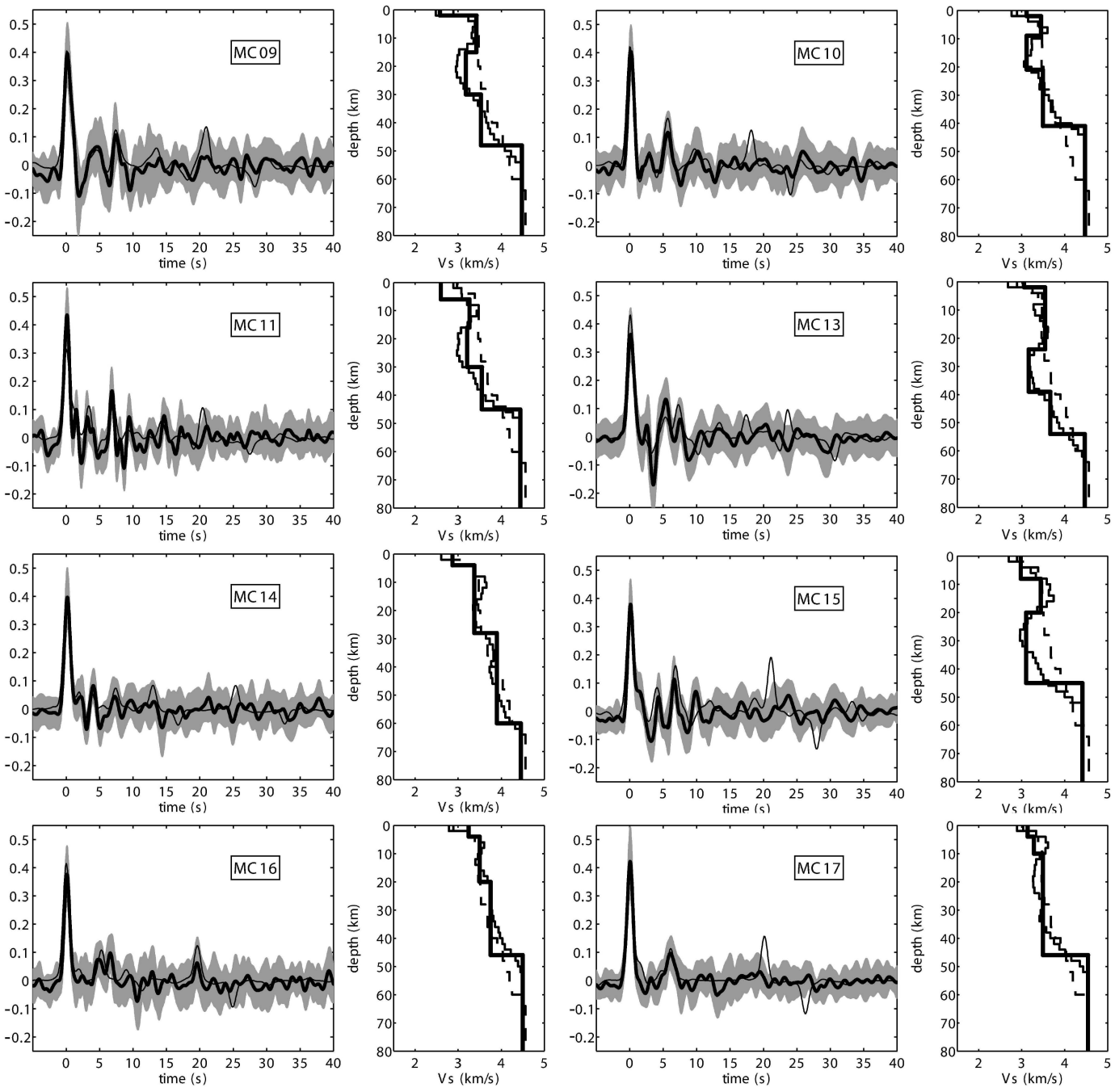

Figure A11 (continued)
Xu et al., 2007

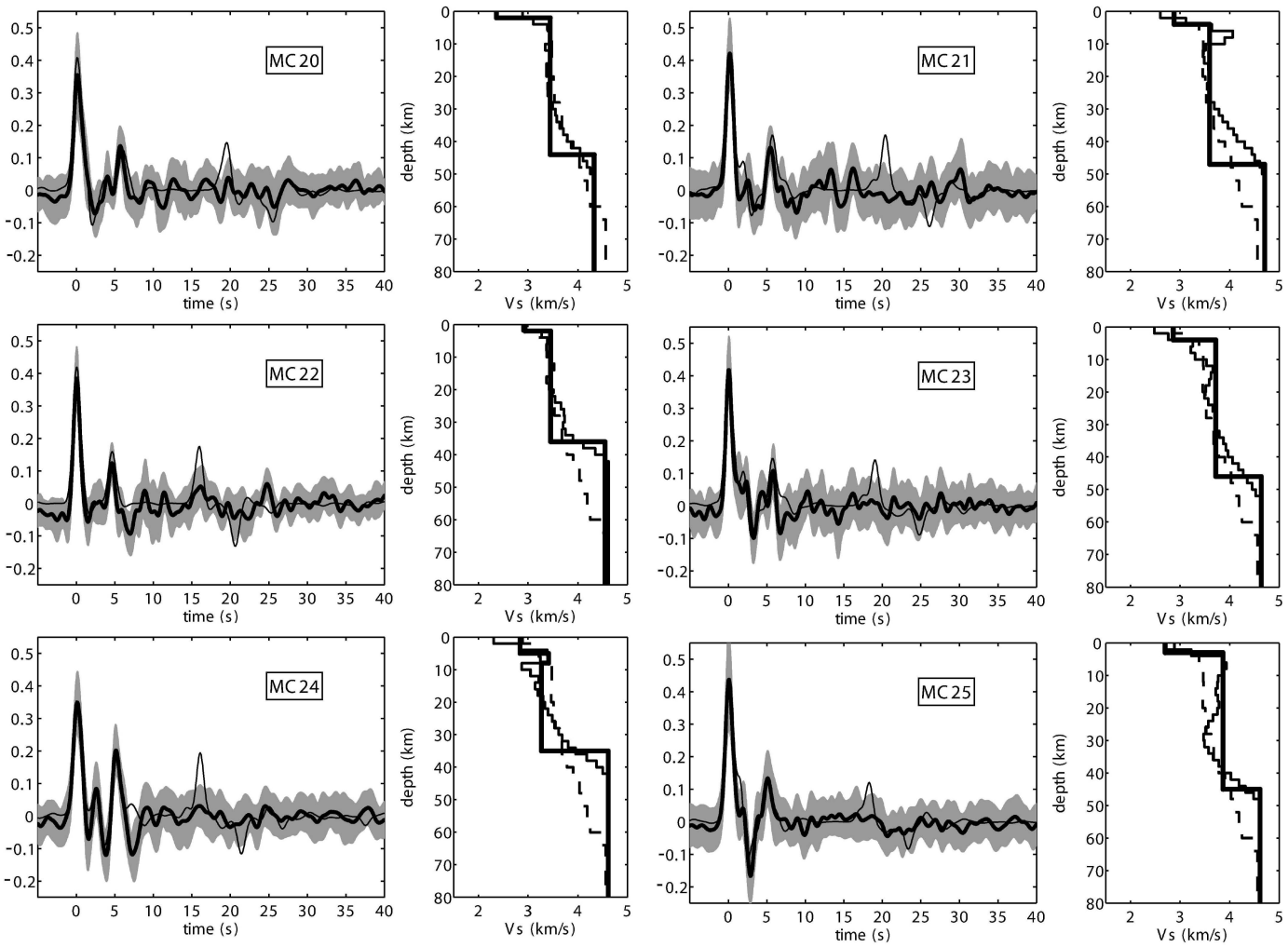

Figure A11 (continued)
Xu et al., 2007

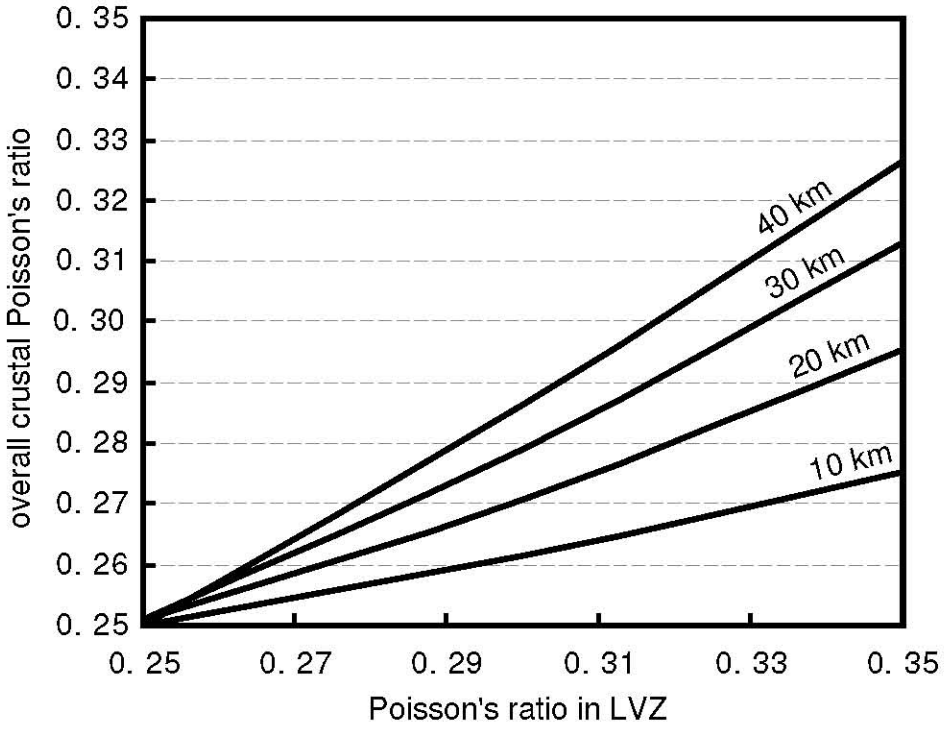

Figure A12
Xu et al., 2007